7-2020

Investigation of the Structural, Electronic, and Thermoelectric Properties of Mono- Chalcogenides

Aida Sheibani
University of Arkansas, Fayetteville

Investigation of the Structural, Electronic, and Thermoelectric Properties of Mono- Chalcogenides

A thesis submitted in partial fulfillment
of the requirements for the degree of
Master of Science in Microelectronics-Photonics

by

Aida Sheibani
Shahed - Tehran University
Bachelor of Science in Physics, 2000
Shahid Beheshti University
Master of Science in Photonics, 2004

July 2020
University of Arkansas

This thesis is approved for recommendation to the Graduate Council.

Bothina Hamad Manasreh, Ph.D.
Dissertation Director

Omar Manasreh, Ph.D.
Committee Member

Laurent Bellaiche, Ph.D.
Committee Member

Rick Wise, Ph.D.
Ex-Officio Member

The following signatories attest that all software used in this thesis was legally licensed for use by Aida Sheibani for research purposes and publication.

Ms. Aida Sheibani, Student	Dr. Bothina Hamad-Manasreh, Thesis Director

This thesis was submitted to http://www.turnitin.com for plagiarism review by the TurnItIn company's software. The signatories have examined the report on this thesis that was returned by TurnItIn and attest that, in their opinion, the items highlighted by the software are incidental to common usage and are not plagiarized material.

Dr. Rick Wise, Program Director	Dr. Bothina Hamad-Manasreh, Thesis Director

Abstract

The structural, electronic, and thermoelectric properties of GeTe are studied using density functional theory and Boltzmann transport equations. This material has a rhombohedral crystal structure in ambient temperature with a ferroelectric behavior due to lack of inversion symmetry. This study suggests that the presence of asymmetry in GeTe can lead to an improvement in the thermoelectric properties of this material. In addition, studies on introducing Group III, IV, and V dopants to GeSe show that while these impurities can improve the power factor and decrease the lattice thermal conductivity, they cannot enhance the figure of merit.

Acknowledgements

First and foremost, praises and thanks to the Lord Almighty for providing this opportunity to study the details of his creation and the wondering beauty behind science. It is with immense gratitude, and profound thanks to, that I acknowledge the support, help, and patience of my adviser, Dr. Bothina Manasreh, who shared with me the great experience of discovery for two years. I would like to express my sincere gratitude to Dr. Charles Paillard for his support, and continuous encouragement. I would like to thank Dr. Omar Manasreh and Dr. Laurent Bellaiche to whom I am very grateful for being on my committee and providing additional assistance toward my degree. I would like to extend my most gratitude and compassion to both Dr. Wise and Renee Jones-Hearon for their unyielding and extremely valuable support through this adventure. I would like to acknowledge my research colleagues Dr. Raad Edaan Haleoot and Mr. Abhiyan Pandit for their technical support for the computation process. I am extremely grateful to my parents for their pure love, prayers, and sacrifices for my education and success. My special thanks goes to my husband, Calbi Gunder, for his belief in my success.

This work was supported by Arkansas NASA EPSCOR Research Infrastructure Development (RID) grant number 002276-00001A. Any opinions, findings, and conclusions or recommendations expressed in this material are those of the author and do not necessarily reflect the views of the Arkansas NASA EPSCOR.

Dedication

This Thesis is dedicated to the big soul of Dr. Farrokh Safavi, beautiful smile of Dr. Rick Wise, and the waiting eyes of my family overseas.

Table of Contents

List of Figures

List of Tables

Chapter 1: Introduction

The excessive use of fossil fuels for public transport and energy generation leads to global climate change. In addition to this problem, the limitation of fossil fuel resources has motivated scientists to search for a way to increase the efficiency of production while limiting the carbon dioxide emission [1]. In most industries, 75% of energy consumption is in the form of thermal energy where 30% of this energy is wasted in the form of discharged heat [2]. Thus, recovery of wasted heat in an environmentally friendly manner can solve a part of these problems. Electrical energy can be extracted from wasted heat by taking advantage of the thermoelectric (TE) modules. Thermoelectric devices are composed of two dissimilar semiconductors that can generate voltage as a result of the temperature difference at both sides of the TE module, in accordance with the Seebeck effect. Oppositely, the heat can be pumped from one side to another by applying an electric current according to the Peltier effect [3]. The direct power generation in thermoelectric materials by the conversion of thermal energy to electric energy is considered to be the most promising technology among other renewable technologies [4]. The pros of TE material are related to the production of low cost and eco-friendly electricity without using moving parts. Different factors can affect the optimal performance of TE devices such as the geometry of the material and operation strategy. In 2005, the research on TE materials was mostly concentrated on cooling application, geometry, shape, size and orientation of the flow in heat transfer systems. Later, other aspects of TE devices such as applicability in electric vehicles have attracted attention [5-7].

As can be deduced from the aforementioned information, TE devices can be used in various technologies, while there are lots of challenges in this field that need to be addressed. The design and assembly of TE devices is still one of the challenging research fields in this area [8].

The efficiency of thermoelectric materials is characterized by the dimensionless figure of

merit $ZT = S^2\sigma/(\kappa_e + \kappa_l)T$, where $S, \sigma, \kappa_e, \kappa_l$ and T are the Seebeck coefficient, electrical conductivity, electrical thermal conductivity, lattice thermal conductivity and temperature, respectively [9]. Typical values of ZT allow to distinguish between inefficient TE materials ($ZT < 1$), TE materials able to harvest waste heat ($ZT \approx 2$), and highly efficient TE materials that are able to match current refrigerators efficiency ($ZT > 4$). Hence, the main focus of the research on TE materials has been devoted to increase the figure of merit ZT [10,11]. An ideal thermoelectric material with high ZT either exhibits a high power factor ($S^2\sigma$) and/or low thermal conductivity ($\kappa_e + \kappa_l = \kappa$). Unfortunately, most of the involved properties of TE materials vary in a competing manner: a low concentration of free carriers tends to increase the Seebeck coefficient but also results in a poor electrical conductivity. Similarly, improving the electrical conductivity causes higher thermal conductivity [12]. Some approaches demonstrate pathways to increase the power factor such as engineering energy degeneracy levels by adopting low dimensional nanostructures, decreasing the bipolar effect [13], or reducing the lattice thermal conductivity by nano structuring [14,15]. Yet, these approaches remain costly and complicated. Thus, finding a good TE material is an important challenge due to the aforementioned restrictions.

Although a variety of materials were studied and investigated for thermoelectric properties, only three of them were marked for mass production: bismuth telluride (Bi_2Te_3), lead telluride (PbTe), and silicon germanium (SiGe) [16]. For a long time, Bi_2Te_3 has been studied and considered as the best thermoelectric material with ZT = 1 and an efficiency ranging from 5 to 7% for most applications at low temperatures. The optimal operating temperature for Bi_2Te_3 is about 450 K and the maximum operating temperature is between 550 and 600 K [11]. Another commercial TE material is lead telluride (PbTe), which works in a moderate temperature range of 350–850 K. The maximum achieved ZT value is about 0.8, which is still insufficient for large-

scale commercial applications [17]. Yet, lead telluride has been in use in many applications such as thermoelectric generators, pacemaker batteries, and even spacecraft vehicles [18]. Despite its success in TE devices, the toxic nature of lead has spurred a significant effort in the search of alternative TE materials. The use of thermoelectric materials in power generation applications and the subsequent interest in finding more efficient TE materials paved the way for the investigation of silicon germanium (SiGe). The advantage of using SiGe is that it has the possibility of forming n-type and p-type materials. This material can operate at a high temperature of the range 800-1300 K and it shows a ZT = 1.3 at 1073 K, which is useful for radioisotope thermoelectric generators [19].

Recently, an experimental work reported an unprecedented ZT of 2.6 at 973 K along the b-axis of bulk SnSe [20]. This groundbreaking work spurred the current interest in IV-VI chalcogenides as promising TE materials, which are capable to work in intermediate temperatures of 600-900 K.

The outline of this dissertation is as follows: Chapter 2 explains the physics behind the thermoelectric effect and the process that result in introducing the figure of merit as an efficiency factor. Chapter 3 presents the density functional theory as a computational methodology for investigating electronic structure. The exchange correlation energy approximation is described, and different kind of exchange correlations are introduced. In Chapter 4, the effect of polar distortion on transport properties of germanium telluride is elucidated and the changing behavior in the lattice thermal conductivity for two polarization levels (1 and 1.5) is demonstrated. In Chapter 5, the electronic and thermoelectric properties of GeS and GeSe are illuminated and the lattice thermal conductivity of these materials are calculated using Slack equation.

Chapter 2: Background

2.1 Thermoelectric

This chapter is devoted to a brief history of different effects that result in the current thermoelectric effect. At the end of this chapter, the steps of deriving efficiency formula and the physics concepts behind this derivation are elaborated.

2.1.1 Seebeck Effect

The first thermoelectric effect was discovered in 1821 by Thomas John Seebeck. He observed that a temperature difference between two dissimilar conductors a and b in an open circuit can create a magnetic field, see Fig. 2.1. At first, he did not recognize that an electric current was induced, and the magnetic field is the result of electric field, so he called this effect the thermomagnetic effect. Hans Christian Ørsted reevaluated the phenomenon and noticed the presence of current and changed the name of this effect to thermoelectricity [21,22]. The relation between the electric field and the temperature gradient is:

$$E = S_{ab} \nabla_r T \qquad \text{(Equation 2.1)}$$

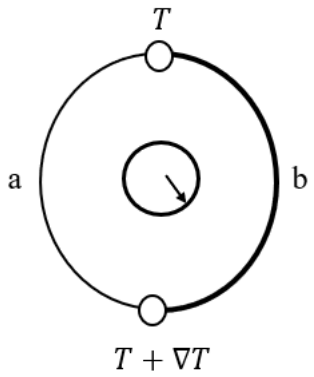

Figure 2.1. Seebeck electric circuit of thermoelectricity.

2.1.2 Peltier Effect and Thomson Effect

The second thermoelectric effect was discovered in 1834 by Jean Charles Athanase Peltier. In this effect, the current flowing through the junction of two different materials a and b produces a temperature gradient in junctions. One junction generates the heat while the other one absorbs it [23]. Thus, the magnitude of absorbed and produced heat is famous as the Peltier coefficient but this magnitude is explained by Lenz [24]. In the Peltier effect, the entropy of the electrical charge carriers changes whenever they pass through a junction and it is not related to external potential. The equation which explains the relation between heat and Peltier effect is as follows:

$$Q = \Pi_{ab} \mathrm{I} \qquad \text{(Equation 2.2)}$$

where Q is the heat that is generated or absorbed, I is the current, and Π_{ab} is the Peltier coefficient for the a and b materials, see Fig.2.2.

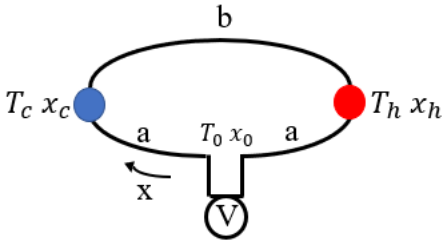

Figure 2.2. Flow in Peltier effect [25].

Seventeen years later, 1851, the Seebeck effect and Peltier effect experiments were repeated by Lord Kelvin. He observed these two experiments are related to each other in a way that the current flowing through a material subject to a temperature difference transfers heat to the environment. Reciprocally, the heat flowing through the material subject to the temperature difference generates an electric current. This effect is famous as the Thomson effect and a simple circuit which shows this effect is illustrated in Figure 2.3. The difference between Thomson,

Seebeck, and Peltier effects is that in the Thomson effect there is only one material while in Seebeck and Peltier effects there are two materials, which are related by a junction. In fact, this effect detects the electric carrier's direction with respect to the temperature in a conductor.

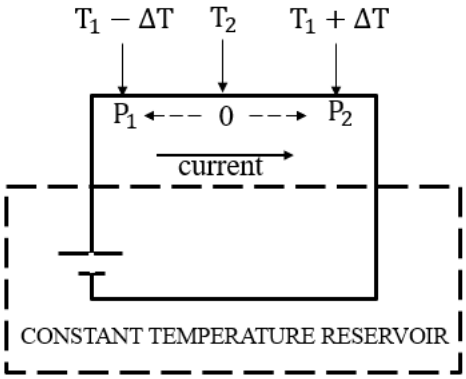

Figure 2.3. Thomson effect [25].

2.1.3 Significance of Figure of Merit

Within the considered temperature range, it is assumed that the variables σ electrical conductivity, S thermopower (Seebeck), and κ thermal conductivity of a material are constant. By this assumption and derivation of conversion efficiency of a system with these properties, the figure of merit is defined using the formula of $Z = \sigma S^2/\kappa$. This section includes the history, system, and the derivation of the efficiency η and extracting Z as a quality factor for evaluating thermoelectric performance of material.

Altenkirch was able to derive a formula that explains the load resistance that results in highest efficiency in thermoelectric generator [26]. In that research, the figure of merit was not extracted, but the role of electrical conductivity σ and thermal conductivity κ in efficiency was described. Another person who worked on thermoelectric generators was Telkes. She did his

research in 1947 and worked on ideal properties of a thermoelectric generator not the figure of merit [27]. In 1952, Ioffe was working on derivation of thermoelectric efficiency that the figure of merit extracted as an effective factor in thermoelectric efficiency [24]. The system that should be considered to derive figure of merit consist of n-type and p-type thermoelements which equally have the length of l. As shown below in Figure 2.4, this circuit is set up in series while thermally it is in parallel. These two dissimilar thermoelements are connected by a conductor with low intrinsic thermal and electrical resistance to make a circuit. These two thermoelements are also connected to each other by a load resistor which is shown by R. The input heat energy is Q_h which enters from the top part and the output heat energy is Q_{c1} and Q_{c2} which come from the bottom of the thermoelement. The temperature difference of $T_h - T_c > 0$ results in temperature flow and generates current of I as the consequence of Seebeck effect.

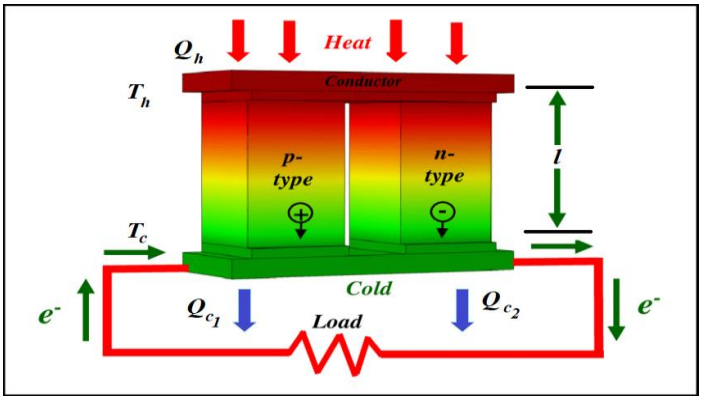

Figure 2.4. A two element thermoelectric generator [28].

In order to derive the formula of thermoelectric efficiency, the electrical conductivity and thermal conductivity of the n-type and p-type thermoelements are equal in temperature range of $T_c \leq T \leq T_h$ which means

$$\sigma_n = \sigma_p = \sigma \quad \text{(Equation 2.3)}$$

$$\kappa_n = \kappa_p = \kappa \quad \text{(Equation 2.4)}$$

The thermopower of these n-type and p-type thermoelements is equal, but with the opposite sign

$$\sigma_n = \sigma_p = \sigma \quad \text{(Equation 2.5)}$$

The cross section of these two thermoelements are considered the same $A_n = A_p = A$.

If the number of thermoelements are equal to N, which half them are n-type and half of them are p-type, with the internal resistance of $r = l/\sigma A$ and thermal conductivity of $k = \kappa A/l$, the generated voltage will be:

$$V = NS(T_h - T_c) = S'\Delta T \quad \text{(Equation 2.6)}$$

By knowing the voltage and considering the internal resistance, which is in series with load resistor, the current can be extracted

$$I = \frac{S'\Delta T}{r + R} \quad \text{(Equation 2.7)}$$

Now it is possible to obtain the power that is delivered to load resistor

$$W = I^2 R = \frac{S'^2 \Delta T^2 R}{(r + R)^2} \quad \text{(Equation 2.8)}$$

In order to get the maximum value of power for the load resistor R, the derivation of Equation 2.8 with respect to R should be equated to zero

$$\frac{dw}{dr} = \frac{S'^2 \Delta T^2 (r + R)^2 - 2(r + R) S'^2 \Delta T^2 R}{(r + R)^4} = 0 \quad \Rightarrow R_{max} = r \quad \text{(Equation 2.9)}$$

So, by substituting Eqn. 2.9 into Eqn. 2.8

$$W_{max} = \frac{S'^2 \Delta T^2 r}{4r^2} \quad , r = Nl/\sigma A$$

$$W_{max} = \frac{NS^2 \Delta T^2}{4\, l/\sigma A} = \Delta T^2 \times \frac{NA}{4l} \times \sigma S^2 \quad \text{(Equation 2.10)}$$

Equation 2.10 clarifies the dependence of maximum power of the thermoelectric generator on

temperature difference (ΔT), design NA/4l, and σS^2 which is famous as the power factor. By dividing the output energy to the input energy, the efficiency of thermoelectric generator can be defined.

At first, the term that is defining the input energy which is the heat that is entering the junction should be written. The heat that is entering can be transferred by thermal conductivity of material, create current and power based on the current that it creates (Seebeck effect), and the internal resistances of the n-type or p-type material do not allow that the whole heat be transferred which explains the negative sign of the last term in following equation

$$Q_h = k\Delta T + S'T_h I - \frac{I^2 r}{2} \quad \text{(Equation 2.11)}$$

By defining the efficiency in equation form

$$\eta = \frac{W}{Q_h} \quad \text{(Equation 2.12)}$$

In order to make the derivation process easier, the ratio of load resistance to internal resistance can be defined as a simple term

$$m = \frac{R}{r} \quad \text{(Equation 2.13)}$$

By substituting Eqn. 2.7 into Eqn. 2.11, and using the Eqn. 2.13 assumption for both W and Q_h then the efficiency will be

$$\eta = \frac{\Delta T}{T_h} \times \frac{\frac{m}{m+1}}{1 + \frac{kr(m+1)}{S'^2 T_h} - \frac{\Delta T}{2T_h(m+1)}} \quad \text{(Equation 2.14)}$$

By defining

$$Z = \frac{S'^2}{kr} = \frac{N^2 S^2}{\frac{N\kappa A}{l}\frac{Nl}{\sigma A}} = \frac{\sigma S^2}{\kappa} \quad \text{(Equation 2.15)}$$

By substitution of Eqn. 2.15 into Eqn. 2.14

$$\eta = \frac{\Delta T}{T_h} \times \frac{\frac{m}{m+1}}{1 + \frac{(m+1)}{ZT_h} - \frac{\Delta T}{2T_h(m+1)}} \qquad \text{(Equation 2.16)}$$

Equation 2.16 shows the efficiency as a function of Z, m, and the temperature difference ΔT. Since the load resistance is an arbitrary factor in designing the thermoelectric power generator, there should be a reasonable reason in choosing the load resistor. There are two option for choosing the load resistance to get the highest efficiency. The first option is choosing the load resistance that results in maximum power which means the numerator of Equation 2.12. The second option is finding derivation of Eqn. 2.16 with respect to m and finding the maximum which leads to

$$R_{\eta max} = rm = r\sqrt{1+ZT} \quad , T = (T_h + T_c)/2 \qquad \text{(Equation 2.17)}$$

ZT is a dimensionless term and is common among researchers on thermoelectrics. By substituting Eqn. 2.17 into Eqn. 2.16, the maximum efficiency for the thermoelectric generator will be obtained.

$$\eta_{max} = \frac{\Delta T}{T_h} \times \frac{\sqrt{1+ZT} - 1}{\sqrt{1+ZT} + \frac{T_c}{T_h}} \qquad \text{(Equation 2.18)}$$

Equation 2.18 sheds light on lots of valuable concepts. It can be deduced that the optimum efficiency relies on temperature difference and the combination of power generation, electrical conductivity, and thermal conductivity. It does not depend on geometry and the number of junctions that can be used in a thermoelectric power generator. This conclusion enlightens the dependence of research in the thermoelectric field on material science.

Chapter 3: Computational Methods

3.1 Quantum Theory

Electrons in materials are responsible for transmitting heat and electricity. Investigation of electrons behavior in a material without quantum theory is impossible. In this chapter, the applied quantum theory and the relation between quantum theory and Boltzman transport theory are presented.

3.1.1 Schrödinger Equation

In quantum mechanics, the wave function describes the quantum states of a system consisting of a set of particles. The wave function of a particle describes the likelihood of the particle being at a given point in a certain space and time. In order to find the wave function of a system, the Schrödinger equation should be solved. The Schrödinger equation can be classified as time dependent Schrödinger equation (Eqn. 3.1) and time independent Schrödinger equation (Eqn. 3.2):

$$i\hbar\frac{\partial\Psi(r,t)}{\partial t} = -\frac{\hbar^2}{2m}\nabla^2\Psi(r,t) + V\Psi(r,t) \qquad \text{(Equation 3.1)}$$

$$\frac{\hbar^2}{2m}\nabla^2\Psi(r,t) + V\Psi(r) = E\Psi(r) \qquad \text{(Equation 3.2)}$$

In equation (3-1) E is replaced by $i\hbar\,\partial/\partial t$ and E is considered independent of time in the second equation. The term $\hbar^2/2m\;\partial^2/\partial x^2$ is called the Hamiltonian, which is nothing more than the total energy of the system in the form of an operation. The Hamiltonian is defined as $H = \hat{T} + \hat{V}$, which is the sum of the kinetic and potential energies. Here the kinetic energy is defined as $T = p^2/2m$, where the momentum is an operator of the form $P = -i\hbar\,\partial/\partial x$. Thus, the Schrödinger equation in

the compact form can be written as:

$$H\Psi = E\Psi \quad \text{(Equation 3.3)}$$

Up to now, the information was mostly about a single particle. For having a real picture about materials, the most stable state of a many-body system should be found, which means the ground state of the system. In order to find the ground state of a many-body system, the many-body Schrödinger equation should be solved. Equation 3.3 shows the compact form of a many-body Schrödinger equation of a general system that consists of N nuclei with the coordinates of R_i and N_e and electrons with coordinates of r_i as follows:

$$H\Psi(\{r_i\},\{R_i\}) = E\Psi(\{r_i\},\{R_i\}) \quad \text{(Equation 3.4)}$$

In many-body problems, the interaction between nuclei-electrons, nuclei-nuclei, and electron-electron should be considered. Using all of these interactions in addition to the kinetic energies of electrons and nuclei, the Hamiltonian can be written as follows:

$$H = T_N(R) + T_e(r) + V_{NN}(R) + V_{Ne}(R,r) + V_{ee}(r), \quad \text{(Equation 3.5)}$$

where $T_N(R)$ is the kinetic energy of the nuclei and can be written as:

$$T_N = \sum_{I=1}^{N} \frac{\hbar^2}{2M_I}\left(\frac{\partial^2}{\partial x_I^2} + \frac{\partial^2}{\partial y_I^2} + \frac{\partial^2}{\partial z_I^2}\right), \quad \text{(Equation 3.6)}$$

where I is the index and shows the number of nuclei and M_I is the effective mass of the nuclei. In Equation 3.6, x, y, and z correspond to the position of nuclei in three dimensions. However, $T_e(r)$ in Equation 3.5 is the kinetic energy of electrons, which can be expressed as:

$$T_e = \sum_{I=1}^{N} \frac{\hbar^2}{2m_i}\left(\frac{\partial^2}{\partial x_i^2} + \frac{\partial^2}{\partial y_i^2} + \frac{\partial^2}{\partial z_i^2}\right), \quad \text{(Equation 3.7)}$$

where i index represents the number of electrons. The effective mass of the electron is denoted by

m_i. In addition, x_i, y_i, and z_i correspond to the position of the electron in three dimensions. Furthermore, the Coulomb interaction between nuclei, V_{NN}, is given as:

$$V_{NN} = \frac{1}{2}\sum_{I}^{M}\sum_{J}^{M}\frac{Z_I Z_J e^2}{|R_I - R_J|} = \frac{1}{2}\sum_{I}^{M}\sum_{J}^{M}\frac{Z_I Z_J e^2}{r_{IJ}}, \quad \text{(Equation 3.8)}$$

In Equation 3.8, Z_I and Z_J represent the atomic number of each nuclei, *e* represents the charge, and r_{IJ} is the distance between them. The $1/2$ ratio in Equation 3.8 is considered to avoid the double counting. The interaction between the nuclei and the electrons can be expressed as:

$$V_{eN} = -\sum_{I}^{M}\sum_{i}^{N}\frac{Z_I e^2}{|R_I - r_i|} = -\sum_{I}^{M}\sum_{i}^{N}\frac{Z_I e^2}{r_{Ii}}, \quad \text{(Equation 3.9)}$$

where r_{Ii} corresponds to the distance between electron *i* and nucleus *I*. Finally, the last term in Equation 3.5 is related to the electron-electron Coulomb interaction, which is given as:

$$V_{ee} = \frac{1}{2}\sum_{i}^{N}\sum_{j}^{N}\frac{e^2}{|r_i - r_j|} = \frac{1}{2}\sum_{i>j}\frac{e^2}{r_{ij}}. \quad \text{(Equation 3.10)}$$

Equation 3.5 is a complex equation with many terms that cannot be solved exactly except for some simple cases such as the hydrogen atom. As a result, applying some approximations is necessary to solve this equation. In the next part, some approximations that can result in simplification will be explained.

3.1.2 Born-Oppenheimmer Approximation

In the Born-Oppenheimmer approximation, it is assumed that nuclei are static due to the fact that the mass of a proton is much larger than the mass of an electron by four orders of magnitude. So, if the nuclei are considered as static, the problem can be limited to the electronic

part, which mathematically means ignoring T_N and V_{NN} due to the heavy mass of nuclei in the denominator of these terms. By taking advantage of the Born-Oppenheimmer approximation, the many-body problem reduces to a many-electron problem, where the Hamiltonian reduces to:

$$H = T_e(r) + V_{Ne}(R, r) + V_{ee}(r). \quad \text{(Equation 3.11)}$$

$$H = \sum_{I=1}^{N} \frac{\hbar^2}{2m_i}\left(\frac{\partial^2}{\partial x_i^2} + \frac{\partial^2}{\partial y_i^2} + \frac{\partial^2}{\partial z_i^2}\right) - \sum_{I}^{M}\sum_{i}^{N} \frac{Z_I e^2}{r_{Ii}} + \frac{1}{2}\sum_{i>j} \frac{e^2}{r_{ij}}. \quad \text{(Equation 3.12)}$$

Therefore, the Schrödinger equation can be simplified as follows:

$$\{T_e(r) + V_{Ne}(R, r) + V_{ee}(r)\}\psi_n^N = E\psi_n^N \quad \text{(Equation 3.13)}$$

As can be seen from Equation 3.13, it is still a many-body problem in accordance to the upper index *N* in the wave function. Solving this problem is not easy, so more approximations, which are explained in next part, are needed to make this equation solvable.

3.1.3 Hartree and Hartree-Fock Approximations

The first approximation to convert the many-body problem to a one-body problem was found by Hartree [29], who suggested to take the wavefunction of the system as the product of the electronic wavefunctions. Thus, the general form of the wavefunction of the many-body system is given as:

$$\psi(\vec{r}_1, \dots, \vec{r}_N, S_1, \dots, S_N) \quad \text{(Equation 3.14)}$$

where $\vec{r}$ is the position of electron and *S* is the spin of electron. For simplicity, consider a two-body system, where the total wavefunction can be written as:

$$\Psi(\vec{x}_1, \vec{x}_2) = \psi_1(\vec{x}_1)|S_1\rangle\psi_2(\vec{x}_2)|S_2\rangle \quad \text{(Equation 3.15)}$$

However, Equation 3.15 is a symmetric wavefunction, which does not satisfy the Pauli exclusion

principle of the electrons that are considered as fermions.

This failure led to Hartree-Fock approximation, which solved the problem by writing the wave function as the combination of Hartree products:

$$\Psi(\vec{x}_1,\vec{x}_2) = \frac{1}{\sqrt{2}}\{\psi_1(\vec{x}_1)|S_1\rangle\psi_2(\vec{x}_2)|S_2\rangle - \psi_1(\vec{x}_2)|S_2\rangle\psi_2(\vec{x}_1)|S_1\rangle\}$$
$$= \frac{1}{\sqrt{2}}\begin{vmatrix}\psi_1(\vec{x}_1)|S_1\rangle & \psi_2(\vec{x}_1)|S_1\rangle \\ \psi_1(\vec{x}_2)|S_2\rangle & \psi_2(\vec{x}_2)|S_2\rangle\end{vmatrix} \quad \text{(Equation 3.17)}$$

Now by extending the two-particle system to a many-body system the wavefunction become:

$$\Psi(\vec{x}_1,\vec{x}_2) = \frac{1}{\sqrt{N!}}\begin{vmatrix}\psi_1(\vec{x}_1)|S_1\rangle & \psi_2(\vec{x}_2)|S_2\rangle \ \dots \ \psi_1(\vec{x}_N)|S_N\rangle \\ \psi_1(\vec{x}_2)|S_2\rangle & \psi_2(\vec{x}_2)|S_2\rangle \ \dots \ \psi_2(\vec{x}_N)|S_N\rangle \\ \vdots & \vdots \qquad\qquad \vdots \\ \psi_N(\vec{x}_1)|S_1\rangle & \psi_N(\vec{x}_2)|S_2\rangle \ \dots \ \psi_N(\vec{x}_N)|S_N\rangle\end{vmatrix} \quad \text{(Equation 3.18)}$$

Each of these wave function can be extracted by solving the following Schrödinger equation:

$$\left(-\frac{\hbar^2}{2m}{\nabla_i}^2 + V\right)\psi_i(\vec{r}) = E_i\psi_i(\vec{r}). \quad \text{(Equation 3.19)}$$

3.1.4 Density Functional Theory

Density functional theory is a quantum mechanical approach for calculating the binding energy of molecules and band structure of solids. The basic idea behind density functional theory was derived by Hohenberg and Kohn [30]. They showed that the ground state properties of a system of many interacting electrons can be viewed as a function of the ground state of electron density which depends on three of spatial coordinates [30]. The Hohenberg-Kohn theory was derived by considering a box consisting of electrons which mutually attract each other by Coulomb repulsion and are affected by external potential. The Hamiltonian for this model can be written as:

$$H = T + U + V, \quad \text{(Equation 3.20)}$$

where *T* is N-electron kinetic energy as mentioned before, and is equivalent with

$$T \equiv \frac{1}{2}\int \nabla\psi^*(r)\int \nabla\psi(r)dr, \quad \text{(Equation 3.21)}$$

U is the electron-electron interaction,

$$U \equiv \tfrac{1}{2}\int \tfrac{1}{|r-r'|}\psi^*(r)\,\psi^*(r')\psi(r')\psi(r)drdr', \quad \text{(Equation 3.22)}$$

and *V* is the potential energy of N-electron from external field,

$$V \equiv \frac{1}{2}\int v(\mathrm{r})\psi^*(r)\,\psi(r)dr. \quad \text{(Equation 3.23)}$$

It should be emphasized that the nondegenerate system is considered for DFT since the degenerate system is described by a time dependent DFT. The electron density based on ground state is defined as:

$$n(r) = N\int d^3r_2 \ldots \int d^3r_N \Psi^*(r, r_2, \ldots, r_N)\Psi(r, r_2, \ldots, r_N) \quad \text{(Equation 3.24)}$$

The wave function is a function of potential energy from external field $v(r)$, which is a unique function of $n(r)$, so all the properties of ground state are unique functionals of $n(r)$ [31]. In the second theorem, Hohenberg and Kohn used the electron density of the system to define the energy functional and showed that by finding the minimum of the energy functional, the ground state energy of the system can be expressed as [31].

$$E = \int v(r)n(r)dr + \tfrac{1}{2}\iint \tfrac{n(r)n(r')}{|r-r'|}drdr' + G[n], \quad \text{(Equation 3.25)}$$

where $G[n]$ is the sum of kinetic energy and exchange correlation energy of an interacting system with n(r), which is expressed as:

$$G[n] \equiv T_s[n] + E_{xc}[n] \quad \text{(Equation 3.26)}$$

Here T_s is the kinetic energy of non interacting electrons and the interacting part is described by

E_{xc} term which is the exchange and correlation energy with density of $n(r)$. The E_{xc} term is the unknown part that will be explained more next.

3.1.5 Exchange Correlation Energy Approximation

The basis of approximation exchange-correlation started from local density approximation (LDA). The model that explains the physics behind the LDA exchange and correlation energy is based on homogeneous electron gas (HEG). In this model, the total ensemble is neutral, since the electron moves on a positive background charge distribution.

If the variation of the charge density (n(r)) is sufficiently slow, the E_{xc} in the LDA approximation can be written as:

$$E_{xc} = \int n(r)\varepsilon_{xc}(n(r))dr \qquad \text{(Equation 3.27)}$$

Here, ε_{xc} is the exchange and correlation energy for each electron in a uniform gas with electron density *n(r)*. In Equation 3.27, the $\varepsilon_{xc}(n(r))$ is considered as a known parameter [32]. A further step is to split the quantity $\varepsilon_{xc}(n(r))$ into two contributions, the exchange and correlation.

$$\varepsilon_{xc}\big(n(r)\big) = \varepsilon_x\big(n(r)\big) + \varepsilon_c\big(n(r)\big), \qquad \text{(Equation 3.28)}$$

where ε_x denotes the exchange part that corresponds to the exchange energy of an electron in a uniform electron gas of a particular density [33].

$$\varepsilon_x\big(n(r)\big) = -\frac{3}{4}\left(\frac{3n(r)}{\pi}\right)^{1/3}, \qquad \text{(Equation 3.29)}$$

However, the correlation part, ε_c, can be obtained using Monte-Carlo simulations [34]. Although LDA exchange correlation was remarkably successful, it has some deficiencies. For

example, it overestimates the cohesive and bond energies and it fails in predicting the ground state energies of iron [35]. These deficiencies in LDA led to more research for finding more accurate exchange energy. In the LDA, the uniform electron gas is taken and is substituted in the constant density in the uniform electron gas with actual density at each point. The next step that was taken to reach more accurate approximation was to include not only the information of density, but also including how the density is changing from one point to other point. By considering this assumption (changes in density) the gradient of density should be included as follows:

$$E_{xc}^{GGA}[n] = \int n(r)\varepsilon_{xc}(n(r), |\nabla n(r)|)dr. \quad \text{(Equation 3-30)}$$

Another class of the exchange-correlation energy approximation is the hybrid functional. This approximation originates from considering the exchange energy of electron with the same spin as the predominant term with high accuracy from Hartree-Fock theory in the total exchange-correlation energy and the rest of the exchange correlation energy from other sources. In this sort of exchange correlation, the effect of self-interaction is neglected [36]. Thus, the exchange-correlation energy can be expressed as follows:

$$E_{xc} = E_x^{exact} + E_c \ , \quad \text{(Equation 3.31)}$$

This approximation gives acceptable results for one center systems such as atoms and ions, but it is inapplicable for description of chemical bonds in molecules [37,38]. The physics behind this situation is related to dynamic correlation (short-range) and nondynamic correlation (long-range) [39]. The Coulomb correlation energy can be modeled as a dynamic component, since the electrons with opposite spin approach one another to short distances.

As a result, the semi-local exchange functionals, which are written as E_x^{DFT} where $DFT = LDA, GGA$ take into account the role of nondynamic correlation and can be written in the compact

form of [40]

$$E_{xc} = E_x^{DFT} + E_c^{DFT} = (E_x^{exact} + E_c^{nd}) + E_c^{DFT} \ , \qquad \text{(Equation 3.32)}$$

By a comparison between Eqn. 3.31 and Eqn. 3.32, it can be deduced that the Eqn. 3.31 is free from self-energy and nondynamic correlation, while Eqn. 3.32 contains both. By considering all aforementioned assumptions, the role of self-interaction and non-dynamic correlation can be considered in a balanced way. In 1993, Becke introduced a linear combination of these functionals based on adiabatic formalism of Kohn-Sham's fictitious system that led to the final form of hybrid exchange correlation functional [41] as:

$$E_{xc}^{hybr} = a_0 E_x^{exact} + (1 - a_0) E_x^{LDA} + a_x \Delta E_x^{B88} + E_c^{LDA} + a_0 \Delta E_c^{GGA}, \qquad \text{(Equation 3.33)}$$

$$a_0 = 0.2 \; a_x = 0.72 \; a_c = 0.81 \; .$$

Here a_0, a_x, and a_c can be obtained by fitting the theoretical results with the experimental results. ΔE_x^{B88} can be obtained from $B88$ functional as a correction to gradient exchange and ΔE_c^{GGA} is a correction to gradient correlation [42].

3.2 Boltzmann Transport Theory for Charge Transport

This section presents the transport properties of the materials. While the macroscopic system is in non-equilibrium, the linear response to driving forces that perturb the equilibrium state is described by near-equilibrium transport phenomena. The distribution function for fermions should be driven to find the coefficients that portray the flux from the driving force. Based on the Boltzmann transport equation, all processes that perturb the equilibrium must net to zero in steady state as follows:

$$\sum \frac{\partial f_{neq}(\boldsymbol{r}, \boldsymbol{k}, t)}{\partial t} \Big|_{process} = 0. \qquad \text{(Equation 3.34)}$$

Here, f_{neq} is the distribution function of a particle at a non-equilibrium state, $\boldsymbol{r}$ is the position, $\boldsymbol{k}$ is the wave vector of the quasi particles, and t is time. By considering time variances in f_{neq} due to diffusion, stationary fields, and scattering, Equation 3.34 can be written as:

$$-v_{\boldsymbol{k}}\frac{\partial f_{neq}}{\partial \boldsymbol{r}}-\frac{\partial \boldsymbol{k}}{\partial t}\frac{\partial f_{neq}}{\partial \boldsymbol{k}}+\frac{\partial f_{neq}}{\partial t}\Big|_{scattering}=0. \qquad \text{(Equation 3.35)}$$

The first term of Eqn. 3.35 refers to the diffusion of the particles or position derivative (first term), the external forces exerted on the particles described by the derivative of momentum (second term), and the scattering described by the last term. The negative signs in the first two terms show the decrease of distribution function at a particular phase space coordinate $(\boldsymbol{r},\boldsymbol{k})$. In order to solve the Boltzmann transport equation, the scattering term should be described specifically.

3.2.1 Relaxation Time Approximation

For subtle changes from equilibrium, the Poisson process can be considered as a model for describing scattering process with a relaxation time τ:

$$\frac{\partial f_{neq}}{\partial t}\Big|_{scattering}=-\frac{f_{neq}-f_{eq}}{\tau}=-\frac{f_{\Delta}}{\tau} \qquad \text{(Equation 3.36)}$$

where f_{Δ} is the subtle linear changes from equilibrium which is denoted by f_{eq}. By using Equation 3.36 and the definition of f_{Δ} in Equation 3.35

$$-v_{\boldsymbol{k}}\frac{\partial(f+f_{\Delta})}{\partial \boldsymbol{r}}-\frac{\partial \boldsymbol{k}}{\partial t}\frac{\partial(f+f_{\Delta})}{\partial \boldsymbol{k}}=\frac{f_{\Delta}}{\tau}. \qquad \text{(Equation 3.37)}$$

The f_{eq} is replaced by Fermi-Dirac distribution function f for fermions:

$$f_{eq}=f=\frac{1}{1+exp\dfrac{E-E_f}{k_bT}} \qquad \text{(Equation 3.38)}$$

where E_f is the electron chemical potential.

3.2.2 Electrical Conductivity

In a stationary electric field, the current density and the direct electrical conductivity are directly proportional to each other as follows:

$$\boldsymbol{J} = \sigma \boldsymbol{E}. \quad \text{(Equation 3.39)}$$

Since σ is linearly proportional to the current density in the Boltzman transport equation the higher order terms like ${\partial f_{\Delta}}/{\partial \boldsymbol{r}}$ and ${\partial f_{\Delta}}/{\partial \boldsymbol{k}}$ are neglected. By considering σ in the limit where there is no temperature gradient, the ${\partial f}/{\partial \boldsymbol{r}}$ can be dropped in Equation 3.37 as follows:

$$-\frac{\partial \boldsymbol{k}}{\partial t}\frac{\partial (f + f_{\Delta})}{\partial \boldsymbol{k}} = \frac{f_{\Delta}}{\tau}. \quad \text{(Equation 3.40)}$$

By considering $qE = \hbar\, \partial \boldsymbol{k}/\partial t$, Equation 3.40 can be written as:

$$f_{\Delta} = -\tau q \frac{1}{\hbar}\frac{\partial f}{\partial \boldsymbol{k}} . \boldsymbol{E} = -\tau q \frac{1}{\hbar}\frac{\partial E}{\partial \boldsymbol{k}}\frac{\partial f}{\partial E} . \boldsymbol{E} = \tau q \left(-\frac{\partial f}{\partial E}\right) v_{\boldsymbol{k}} . \boldsymbol{E}, \quad \text{(Equation 3.41)}$$

where E is the energy of the carrier and $\boldsymbol{E}$ (bold font weight shows the vector quantities) is the electric field. By defining the flux as the product of the velocity of particles and the volume density of these particles, the charge density equation can be defined as:

$$J = q \int_{BZ} v_{\boldsymbol{k}} f_{neq} = q \int_{BZ} v_{\boldsymbol{k}} (f + f_{\Delta}) = q \int_{BZ} v_{\boldsymbol{k}} f_{\Delta}. \quad \text{(Equation 3.42)}$$

The velocity is dependent on $\boldsymbol{k}$, so the $\boldsymbol{k}$ is used as an index for v. The flux in the equilibrium is zero so $\int_{BZ} v_{\boldsymbol{k}} f = 0$. By substituting Equation 3.41 into Equation 3.42 and using the linear relation of charge density and electrical conductivity, $\boldsymbol{J} = \sigma \boldsymbol{E}$, the equation of electrical conductivity becomes:

$$\sigma_{ij} = q^2\tau \int_{BZ} v_{k,i}\, v_{k,j} \left(-\frac{\partial f}{\partial E}\right) = \frac{q^2}{4\pi^3}\tau \int_{BZ} v_{k,i}\, v_{k,j} \left(-\frac{\partial f}{\partial E}\right) d^3k. \quad \text{(Equation 3.43)}$$

In Equation 3.43, the volume of k space is considered, and spin degeneracy is substituted. Due to the fact that $\boldsymbol{k}$ and E are related through band dispersion relation, Equation 3.43 can be written in terms of energy as:

$$\sigma_{xx} = e^2 \int \tau(E)\, v_x^2(E) \left(-\frac{\partial f}{\partial E}\right) g(E) dE, \quad \text{(Equation 3.44)}$$

where $g(E)$ is the density of states and q is substituted with $\pm e$.

3.2.3 Seebeck Coefficient

It is possible to drive electric current and electric field by temperature gradient. The Seebeck coefficient, S, describes the proportionality between the thermal gradient and electric field in an open circuit as:

$$S = -\frac{\nabla V}{\nabla T}. \quad \text{(Equation 3.45)}$$

In this equation, $-\nabla V = \boldsymbol{E}$ is the electric potential gradient, which is in the same direction as the thermal gradient. In order to derive S, the Boltzmann tranport equation should be used again by considering the thermal gradient:

$$-v_{\boldsymbol{k}} \frac{\partial (f + f_\Delta)}{\partial \boldsymbol{r}} = -v_{\boldsymbol{k}} \frac{\partial f}{\partial \boldsymbol{r}} = \frac{f_\Delta}{\tau}. \quad \text{(Equation 3.46)}$$

The ${\partial f_\Delta}/{\partial r}$ is neglected.

$$\frac{\partial f}{\partial \boldsymbol{r}} = \frac{\partial f}{\partial T}\frac{\partial T}{\partial \boldsymbol{r}} = \frac{\partial f}{\partial T}\nabla T. \quad \text{(Equation 3.47)}$$

By considering the Fermi-Dirac distribution function f and taking the derivative with respect to

$\partial f / \partial T$

$$\frac{\partial f}{\partial T} = \frac{E - E_f}{T}\left(-\frac{\partial f}{\partial E}\right). \quad \text{(Equation 3.48)}$$

By substituting Equations 3.47 and 3.48 into 3.46 leads to:

$$f_\Delta = -\tau \frac{E - E_f}{T}\left(-\frac{\partial f}{\partial E}\right) v_{\boldsymbol{k}}.\nabla T. \quad \text{(Equation 3.49)}$$

Substituting the thermal gradient term in current density and considering the current density under electric field:

$$\boldsymbol{J} = -q\int_{BZ} \tau v_{\boldsymbol{k}} v_{\boldsymbol{k}} \frac{E - E_f}{T}\left(-\frac{\partial f}{\partial E}\right)\nabla T - \sigma \nabla \mathrm{V}. \quad \text{(Equation 3.50)}$$

In an open circuit $\boldsymbol{J} = 0$, so the Seebeck coeficient can be extracted out as:

$$S_{xx} = \frac{q}{\sigma_{xx}}\int_{BZ} \tau v_x v_x \frac{E - E_f}{T}\left(-\frac{\partial f}{\partial E}\right) d^3k. \quad \text{(Equation 3.51)}$$

Again, by referring to the relation between $\boldsymbol{k}$ and E through the dispersion relation, Equation 3.51 can be written as:

$$S_{xx} = \frac{k_B q}{\sigma_{xx}}\int_{BZ} \tau v_x v_x \frac{E - E_f}{k_B T}\left(-\frac{\partial f}{\partial E}\right) g(E) dE. \quad \text{(Equation 3.52)}$$

As a result, the Seebeck coefficient is an odd function with respect to the E_f

Chapter 4: Effect of Polar Distortion on Thermoelectric Properties of GeTe

4.1 Introduction

Germanium telluride is analogous to one of the prototype thermoelectric materials, namely PbTe, which exhibits high-performance thermoelectric properties. This material is a promising alternative for PbTe due to the non-toxic nature (Pb free structure), which attracted a lot of attention from the thermoelectric community [43,44]. Different facets of thermoelectric properties of GeTe, which can directly and indirectly affect the TE efficiency, have been intensively investigated. For instance, the band structure of this material in rhombohedral and cubic structures was comprehensively studied and the effect of degeneracy and band valleys on thermoelectric properties have been described in detail [45]. The TE properties and the figure-of-merit of GeTe as a function of temperature have been already reported for the three different phases [46]. The decoupling between the Seebeck coefficient and electrical conductivity in p-type rhombohedral and cubic GeTe by taking advantage of the electronic fitness function (EFF) was explored [47]. Experimentalists attempted to decrease the Curie temperature from 700 K to 300 K by Bi and Mn co-doping [44]. The effect of different doping species on GeTe have been investigated extensively both theoretically and experimentally [48-52]. Due to the high amount of Ge vacancies, recent experimental studies focused on decreasing the vacancy in this material through optimizing the amount of GeTe, which significantly enhanced the ZT value from 1 to 2 [53,54].

One aspect that has been clearly overlooked in all these studies is the effect of ferroelectricity on thermoelectric properties of this material in the rhombohedral phase. In ambient conditions, GeTe has indeed a rhombohedral structure (*R3m* space group), which is ferroelectric [47,55-57]. In other words, GeTe possesses a spontaneous electrical polarization that can be reversed by applying an external electric field. The phase of GeTe transfers to a cubic paraelectric structure when heated above a critical temperature between 600 and 700 K, depending on the doping level [47,55-57]. It thus appeared that

there is a need to disentangle the various degrees of freedom (such as polarization) in order to better understand and engineer the TE properties of GeTe. To this end, *ab initio* calculations of electronic band structure and thermoelectric properties of bulk GeTe are reported in this thesis.

4.2 Computational Methodology

First-principle electronic structure calculations based on Kohn-Sham density functional theory (DFT) are performed using the Vienna ab initio simulation package (VASP) to obtain the electronic and structural properties of GeTe alloy [58]. Based on the DFT results, the thermoelectric properties were calculated using semi-classical Boltzmann transport theory using BoltzTrap code [59], which relies on Fourier expansion to find an appropriate fit of the band energies to calculate the transport properties. The iterative solution of phonon BTE using ShengBTE code was used to calculate the lattice thermal conductivity.

The generalized gradient approximation in the formal Perdew–Burke–Ernzerhof (PBE) parametrization scheme was used to describe the exchange correlation energy of electrons. The kinetic plane wave cut-off was chosen as 520 eV, and the Brillouin zone (BZ) was meshed using a $12 \times 12 \times 12$ Γ-centered grid. The lattice parameters and ionic positions were optimized using a force convergence criterion of 0.01 eV/Å. The electronic band structure obtained from first-principles is interpolated on a denser k-mesh of $60 \times 60 \times 60$ to calculate the thermoelectric properties. By defining the group velocity term as:

$$v_\alpha(i, \boldsymbol{k}) = \frac{1}{\hbar}\frac{\partial \varepsilon_{i,k}}{\partial k_\alpha}, \qquad \text{(Equation 4.1)}$$

the conductivity tensors can be shown as:

$$\sigma_{\alpha\beta}(i, \boldsymbol{k}) = e^2 \tau_{i,\boldsymbol{k}} v_{\alpha\beta}(i, \boldsymbol{k}) v_\beta(i, \boldsymbol{k}), \qquad \text{(Equation 4.2)}$$

where e is charge and τ is the relaxation time.

The energy projected conductivity tensors can be defined using conductivity tensors:

$$\sigma_{\alpha\beta}(\varepsilon) = \frac{1}{N}\sum_{i,k}\sigma_{\alpha\beta}(i,\boldsymbol{k})\frac{\delta(\varepsilon-\varepsilon_{i,k})}{\partial k_{\alpha}}. \quad \text{(Equation 4.3)}$$

The Seebeck coefficient, electrical conductivity tensors in the semi-classical transport theory are as follows [60]:

$$\sigma_{\alpha\beta}(T,\mu) = \frac{1}{\Omega}\int \sigma_{\alpha\beta}(\varepsilon)[-\frac{\partial f_0(T,\varepsilon,\mu)}{\partial\varepsilon}]d\varepsilon, \quad \text{(Equation 4.4)}$$

$$S_{\alpha\beta}(T,\mu) = \frac{1}{eT\sigma_{\alpha\beta}(T,\mu)}\int \sigma_{\alpha\beta}(\varepsilon)(\varepsilon-\mu)[-\frac{\partial f_0(T,\varepsilon,\mu)}{\partial\varepsilon}]d\varepsilon\,, \quad \text{(Equation 4.5)}$$

where e is the electron charge, T is the absolute temperature, Ω is the volume of the reciprocal space, f is the Fermi distribution function, ε is the carrier energy, and μ the chemical potential. This method is based on the relaxation time approximation (RTA), which means that the relaxation time is treated as a constant. The relaxation time is set to the value of $\tau = 1.0 \times 10^{-14}$ s for calculating the figure-of-merit [61].

To investigate the stability of the structure in different polar states, the phonon dispersion and second order harmonic interaction force constants are calculated in a $4 \times 4 \times 4$ supercell and *k*-mesh of a $3 \times 3 \times 3$ with the Phonopy package [62]. The third order harmonic interaction force constants are calculated using the third.py module of the ShengBTE package [60] and a $4 \times 4 \times 4$ supercell up to fourth nearest neighbors was used to calculate lattice thermal conductivity.

4.3 Results and Discussion

This section presents structural, electronic, and transport properties of the cubic ($Fm\bar{3}m$) and the rhombohedral (*R3m*) structures of GeTe alloy (at different levels of polarization).

4.3.1 Structural Properties

In this sub-section, the structural properties of GeTe are summarized. This material has allotropic structures, such as *R3m*, *P1*, *Cm*, and $Fm\bar{3}m$, where the first three structures may coexist at room temperature, whereas $Fm\bar{3}m$ exists at temperatures above 680 K [63]. The rhombohedral (so-called $\alpha - \mathrm{GeTe}$) structure is known to be the most stable structure in the temperature range 300-600 K. This structure is pictured in Figure 4.1.

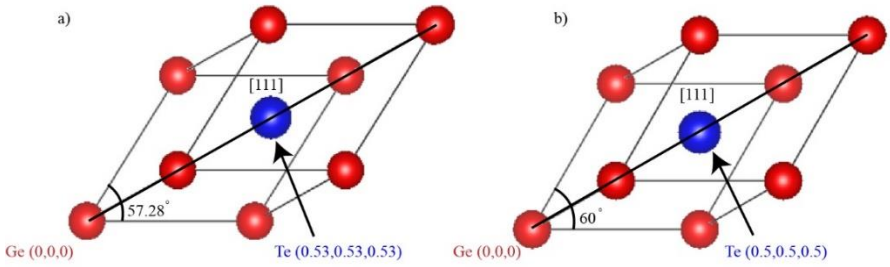

Figure 4.1. Primitive cell of GeTe (a) rhombohedral (R3m), (b) cubic ($Fm\bar{3}m$) phases. Red and blue sphere represent Ge and Te atoms, respectively.

Germanium telluride in rhombohedral phase is a ferroelectric material [56]. It is characterized by a polar distortion where the Ge and Te atoms are displaced from their high symmetry position of (0,0,0) and (1/2,1/2,1/2), respectively, along the [111] crystallographic direction (see Fig. 4.1). As a result, their general position in the ferroelectric ground state can be denoted as $r_{Ge} = (0,0,0) + (\delta_{Ge}, \delta_{Ge}, \delta_{Ge})$ and $r_{Te} = (\frac{1}{2},\frac{1}{2},\frac{1}{2}) + (\delta_{Te}, \delta_{Te}, \delta_{Te})$, where $\delta_{Ge} = -0.0057136$ and $\delta_{Te} = 0.026713$ are the distortions in the ground state. We studied the effect of changing the polarization on the thermoelectric properties by varying the amplitude of the ferroelectric distortion. Specifically, we studied structures with the Ge and Te atoms fixed at the positions $r_{Ge} = (0,0,0) + \lambda(\delta_{Ge}, \delta_{Ge}, \delta_{Ge})$ and $r_{Te} = (\frac{1}{2},\frac{1}{2},\frac{1}{2}) + \lambda(\delta_{Te}, \delta_{Te}, \delta_{Te})$, where $\lambda = 1$

and $\lambda = 0$ represents the rhombohedral polar ground state and the rhombohedral non-polar state, respectively. The interaxial angle (α) was kept the same as that of the rhombohedral polar ground state structure.

The calculated lattice parameters for the ground state rhombohedral structure of GeTe ($\lambda = 1$) are: $a = 4.41$ Å and $\alpha = 57.28^{\circ}$, (see Table 4.1.). From this table, one can see that the calculated lattice parameter of the rhombohedral GeTe agrees with previous DFT calculations within a percentage difference of 2% [46,64]. It is also in fair agreement with the experimental findings using x-ray diffraction (XRD) and Raman analyses within 3-4% [63]. The calculated interaxial angle is found to differ from previous calculations by 1% and from the experimental results by 2-3% [46,56], see Table 4.1. The lattice parameters for the cubic primitive cell of GeTe are: $a = 4.25$ Å and $\alpha = 60^{\circ}$. The calculated interaxial angle is exactly as reported in previous calculations, whereas the lattice parameter differs by 0.23 - 1% [63,65].

Table 4.1. Comparison of calculated lattice parameters (present work) of GeTe with other theoretical and experimental reports

System	Work	a (Å)	Interaxial angle (°)	Eg (eV)
R3m	Present	4.41	57.28	0.55
	Other	4.32[a] -4.41[b]	57.7[c]-58.08[b]	0.70[b]-0.80[d]
	Experiments	4.24-4.27[d]	58.62-58.97[d]	0.55[e]
$Fm\bar{3}m$	Present	4.25	60	0.35
	Other	4.18[d]-4.26[f]	60[d]	0.34[d]

[a] Reference [46], [b] Reference [64], [c] Reference [56], [d] Reference [63], [e] Reference [66], [f] Reference [65].

4.3.2 The Electronic Structure

This subsection presents the band structure and the density of states of rhombohedral and cubic structures of GeTe. The electronic band gap is determined as the difference between the valence band maximum (VBM) and the conduction band minimum (CBM). Figure 4.2 (a) presents the band structure and the density of states of the rhombohedral structure in its ground state (*i.e.* λ=1). This structure exhibits an indirect band gap of 0.55 eV (VBM is at the Σ point between P and Γ and CBM is at L), which is, thus, of the same nature as the reported experimental band gap [66]. By imposing a distortion $\lambda = 0$ (i.e. non-polar state), the band gap is significantly reduced to 0.165 eV. Interestingly, it decreases further to 0.005 eV when $\lambda = 0.3$ (i.e. polarization approximately reduced by 70% with respect to the ground state) after which the band gap increases steadily up to 0.558 eV for $\lambda = 0.7$ (polarization reduced by 30%) (see Figure 4.3). However, the changes in the band gap are not significant for higher ferroelectric distortions ($\lambda \geq 0.7$). In contrast, a direct band gap of 0.35 eV is obtained for the cubic GeTe structure (see Figure 4.2 (c)), in agreement with previous calculations (0.34 eV) [63].

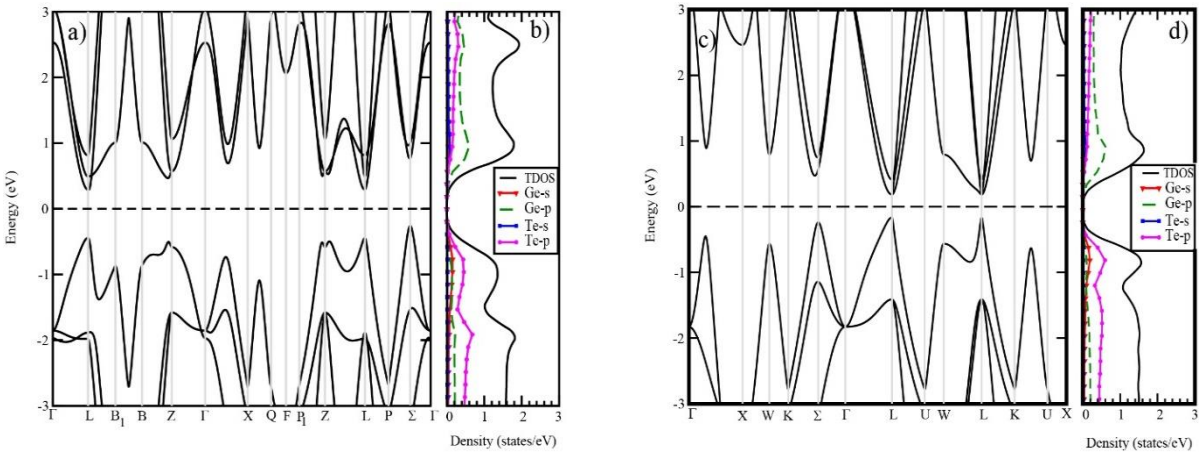

Figure 4.2. The electronic band structure (a) ground state rhombohedral (c) cubic, and density of states of (b) rhombohedral (d) cubic GeTe.

The total and projected density of states TDOS and PDOS, are presented in Figure 4.2 (b) and Figure 4.2 (d) for rhombohedral and cubic phases, respectively. The Te *p*-orbitals dominate the valence bands, while the conduction bands are dominated by Ge *p*-orbitals. The density of states plots of both structures have sharp peaks near the conduction band minima and valence band maxima, which promises to lead to higher Seebeck coefficients values near the band edges. However, the rhombohedral phase shows higher peaks in the density of states, which indicates higher Seebeck coefficient values than those of the cubic phase.

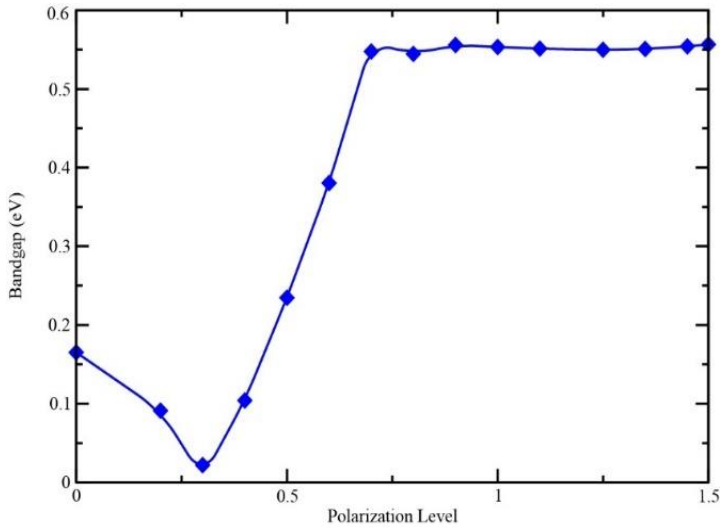

Figure 4.3. The band gap as a function of the polarization level of rhombohedral GeTe structure.

4.3.3 Thermoelectric Properties

The Seebeck coefficient (*S*) characterizes the ability to produce a voltage from the temperature gradient existing in a material. Figure 4.4 presents the Seebeck coefficient, *S*, as a function of the chemical potential μ (which is plotted with respect to the Fermi energy, E_f), for the most stable structure ($\lambda = 1$), at different temperatures below the transition temperature. This figure shows that the Seebeck coefficient decreases as the temperature increases for chemical

potentials close to the Fermi energy (approximately for μ laying within the bandgap). This is due to concurrent excitation of intrinsic free holes and electrons across the bandgap, which contributes oppositely to the Seebeck coefficient (the so-called bipolar effect) [67]. Therefore, the highest Seebeck coefficient values are found at low temperatures. For instance, at 300 K, maximum values of 1055 μV/K and 986 μV/K are found for *p*- and *n*-type doping, respectively. The values of the Seebeck coefficient increase rapidly near the Fermi energy, which indicates that the highest values can be obtained for low carrier concentrations of the *n*- and *p*-type doping. This behavior is related to the fact that the Seebeck coefficient is proportional to $T\,{}^{\partial \ln(N(E))}/_{\partial E}$ [68], where $N(E)$ is the electronic density of states and T the temperature. The large slope of the DOS near the band edges in Figure 4.2 (b) is thus responsible for the large enhancement of the Seebeck coefficient for μ values close to the band edges, as well as the temperature dependency of the Seebeck coefficient.

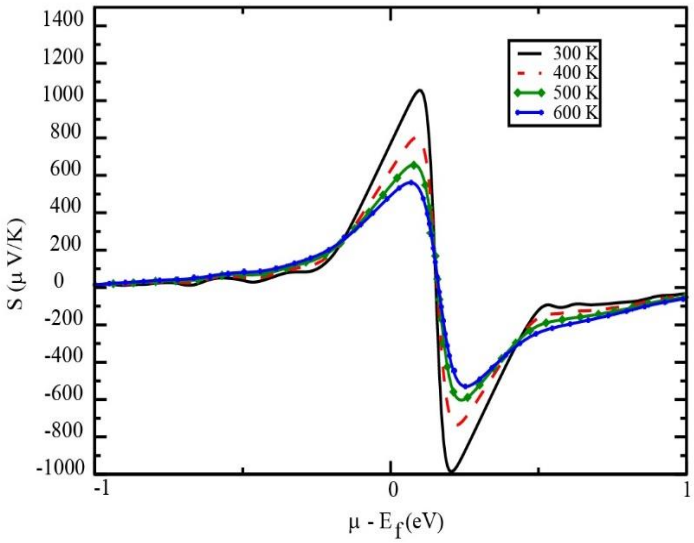

Figure 4.4. The Seebeck coefficient as a function of the chemical potential deviation from the Fermi level for the ground state rhombohedral structure ($\lambda = 1$), at 300 K, 400 K, 500 K, and 600 K

Calculations using various ferroelectric distortions, λ ($\lambda = 0, 0.5, 1.0, 1.25, 1.5$), at fixed cell geometry are performed to understand the effect of the electrical polarization on the thermoelectric properties. The Seebeck coefficient at different polarization levels is presented in Figure 4.5 at two temperatures of 300 K and 600 K.

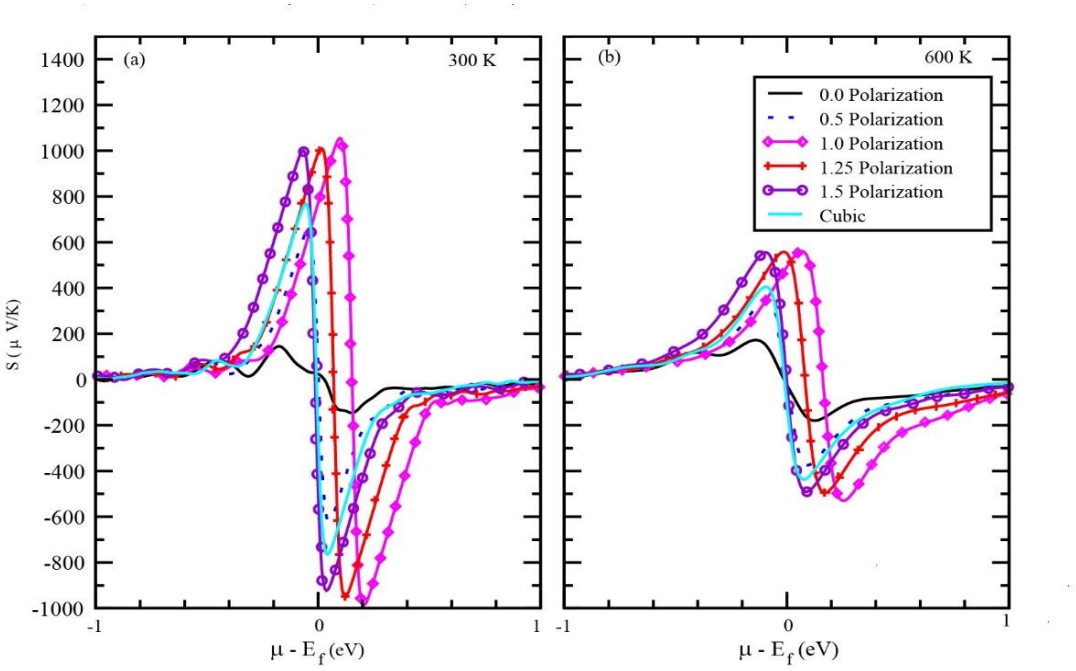

Figure 4.5. The Seebeck coefficient as a function of the chemical potential deviation from the Fermi level for the rhombohedral structure at 0.0, 0.5, 1.0, and 1.25 polarizations in addition to the cubic structure at (a) 300 K and (b) 600 K.

From Figure 4.5, it appears clear that the Seebeck coefficient is greatly reduced when the polarization is reduced. For vanishing polarization ($\lambda = 0$), the extrema of the Seebeck coefficient are reduced by an order of magnitude as compared to the polar ground state ($\lambda = 1$). For 0.5 polarization, the Seebeck coefficient shows a maximum at 647 μV/K for *p*-doping and 620 μV/K for *n*-doping near the Fermi level at 300 K. By increasing the polarization from 0.5 to 1.0, the maximum value of the Seebeck coefficient at 300 K increases to 1055 μV/K for *p*-type doping and

986 μV/K for *n*-type doping. Interestingly, there is a slight decrease in the Seebeck coefficient peaks for polarization levels beyond 1.0. It is obvious from Figure 4.5 (a) and (b) that the Seebeck coefficient decreases when the temperature increases, as discussed before. The peak value of *S* at 600 K for the polarization level of 0.5 is 349 μV/K and 374 μV/K for *p*-type and *n*-type doping, respectively. Figure 4.6 summarizes the effect of the polar distortion on the Seebeck coefficient (at 300 K). This figure shows a steady increase in the Seebeck coefficient until the polarization state reaches that of the ground state. Beyond that point, the Seebeck coefficient reaches a plateau.

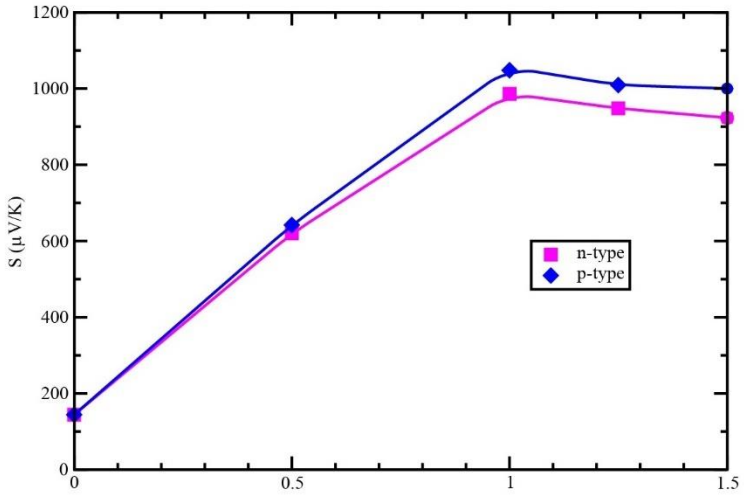

Figure 4.6. Seebeck peaks as a function of polarization level in 300 K.

The Seebeck coefficient is also calculated for the cubic structure without polarization (see Figure 4.5). In this case, the peaks of the Seebeck coefficient are 531 μV/K and 613 μV/K for *p*-type and *n*-type doping, respectively, which are much higher than those of the non-polar ($\lambda = 0$) rhombohedral structure at 300 K. However, these values remain smaller by 4% as compared to the rhombohedral polar ground state structure. By increasing the temperature of the cubic structure to

600 K, the Seebeck coefficient peak values decrease to 373 μV/K and 364 μV/K for *p*-type and *n*-type doping, respectively.

Attention is now turned to the electronic properties (namely the electrical conductivity) of GeTe. The semi-classical Boltzmann transport theory of electrical conductivity σ depends linearly on a relaxation time τ. This dependency can be expressed as:

$$\sigma = \frac{ne^2\tau}{m^*}, \qquad \text{(Equation 4.6)}$$

where *n* is the free carrier concentration, *e* is the charge carrier, and m^* is the free carrier effective mass. Due to phonon scattering by defects and boundaries, it is difficult to determine the relaxation time in bulk materials [69] [70]. Thus, a constant relaxation time is assumed to calculate σ. Figure 4.7 presents the σ/τ ratio as a function of the deviation of the chemical potential (μ) from the Fermi-level (E_f) at different temperatures (300 – 600 K), in the polar ground state structure ($\lambda = 1$).

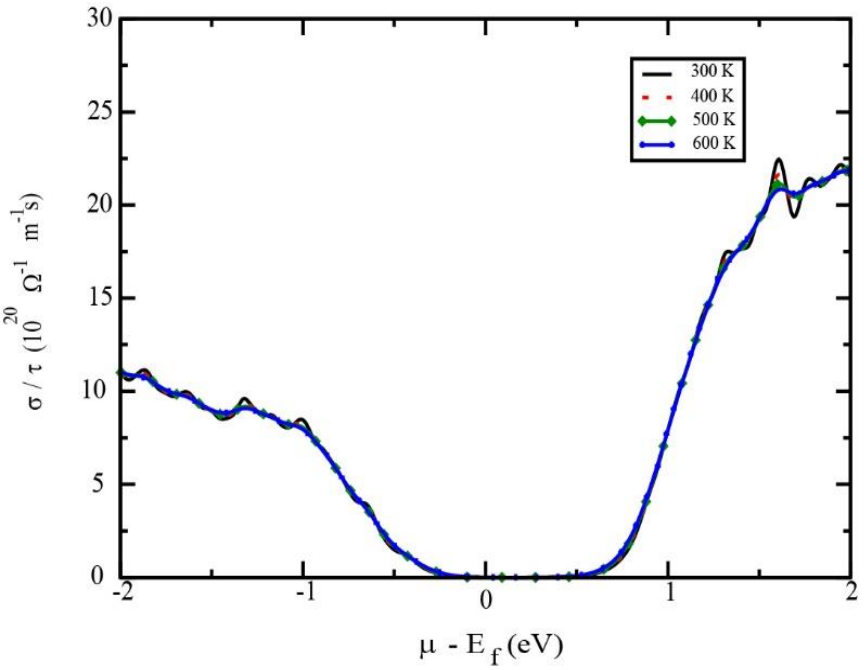

Figure 4.7**:** The electrical conductivity as a function of deviation of the chemical potential from Fermi level in 300 K, 400 K, 500 K, and 600 K.

From this figure, one can see that the electrical conductivity, σ, is almost independent of temperature. As can be seen in Figure 4.7 when comparing chemical potentials close to the valence band edge or close to the conduction band edge, electronic conductivity is larger than hole conductivity. By comparing Figure 4.5 and 4.7, one can see that the electrical conductivity is very small when the Seebeck coefficient reaches its peak value and vice versa. Thus, there exists a particular Fermi level μ and a particular doping concentration that optimizes the power factor ZT to accommodate for those two competing effects.

The electrical conductivity is also studied for different magnitudes of the polarization as depicted in Figure 4.8. (a) and (b). This figure shows that the electrical conductivity decreases whenever the polarization increases. Note that the highest electrical conductivity is achieved for the rhombohedral distortion without polarization ($\lambda = 0$); meanwhile, the non-polar cubic structure has the same order of magnitude of the conductivity as the polar rhombohedral ground state ($\lambda = 1$). It is even a slightly better conductor for chemical potentials near the valence band edge.

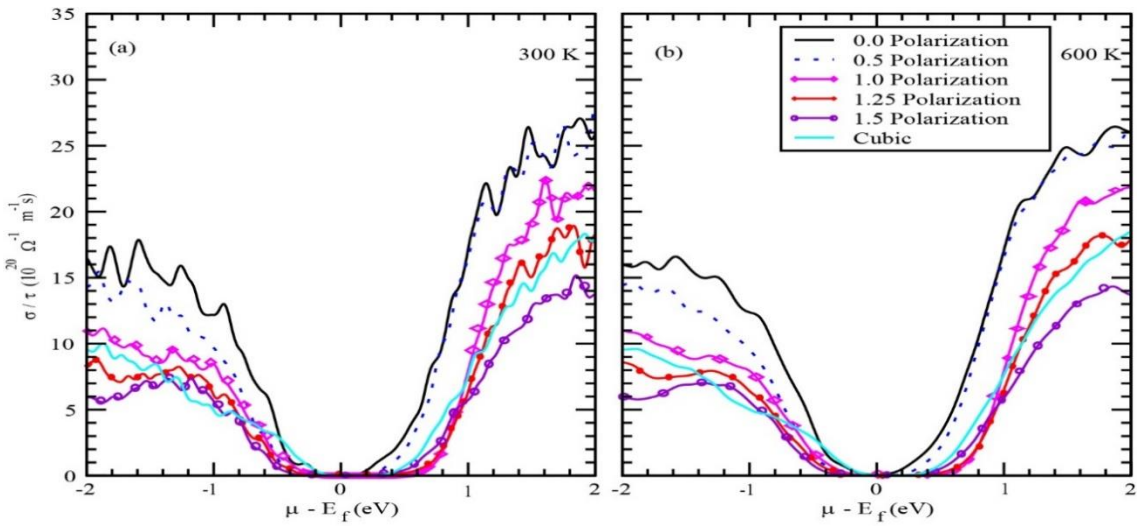

Figure 4.8. The electrical conductivity as a function of deviation of the chemical potential from Fermi level in (a) in 0.0 polarization, 0.5 polarization, 1.0 polarization, 1.25 polarization, 1.5 polarization, and Cubic GeTe in 300 K and (b) 600 K.

The electrical conductivity (σ) and electronic thermal conductivity (κ_e) are directly proportional according to Weidemann-Franz law ($\kappa_e = L\sigma T$) [71]. The electronic thermal conductivity is thus, not surprisingly, following similar trends as the electrical conductivity for different levels of polarization. The electronic thermal conductivity (κ_e/τ) increases as the temperature increases. Consistently with the electrical conductivity data, the electronic thermal conductivity of cubic GeTe near the band gap is also higher than that of the rhombohedral structure at polarization levels of 1.0, 1.25, and 1.5 (see Figure 4.9).

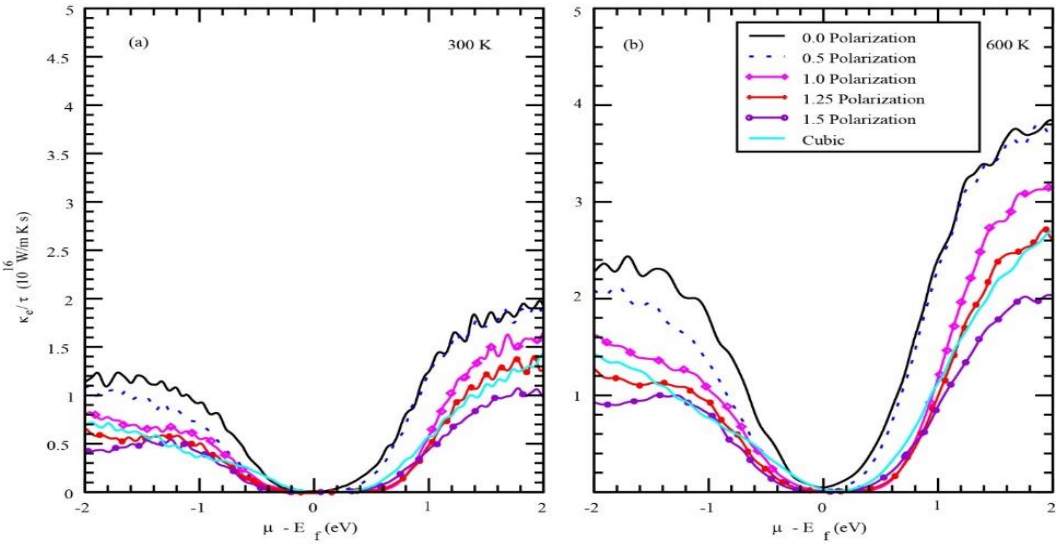

Figure 4.9. The electronic thermal conductivity as a function of the chemical potential deviation from Fermi level in 0.0 polarization, 0.5 polarization, 1.0 polarization, 1.25 polarization, and Cubic GeTe at (a) 300 K and (b) 600 K.

Although all transport properties were separately described, focus was placed on trying to mend all the previously mentioned notions in a single descriptor, the so-called figure of merit ZT. However, this quantity depends on the relaxation time, which is very difficult to calculate accurately from first-principle calculations. Thus, another quantity, ZT_e, was introduced which can be understood as an electronic figure of merit that is related to ZT as follows:

$$ZT = \frac{S^2\sigma \mathrm{T}}{\kappa_e}\frac{\kappa_e}{\kappa_e + \kappa_{latt}} = \mathrm{ZT_e}\frac{\kappa_e}{\kappa_e + \kappa_{latt}}. \quad \text{(Equation 4.7)}$$

In addition, low polarization states ($\lambda = 0.5$ and 0), as well as the cubic structure, show some imaginary phonon frequencies (optical soft-modes characteristic of the ferroelectric instability, see Figure 4.10) which prevent the proper calculation of the lattice thermal conductivity for these materials, κ_{latt}.

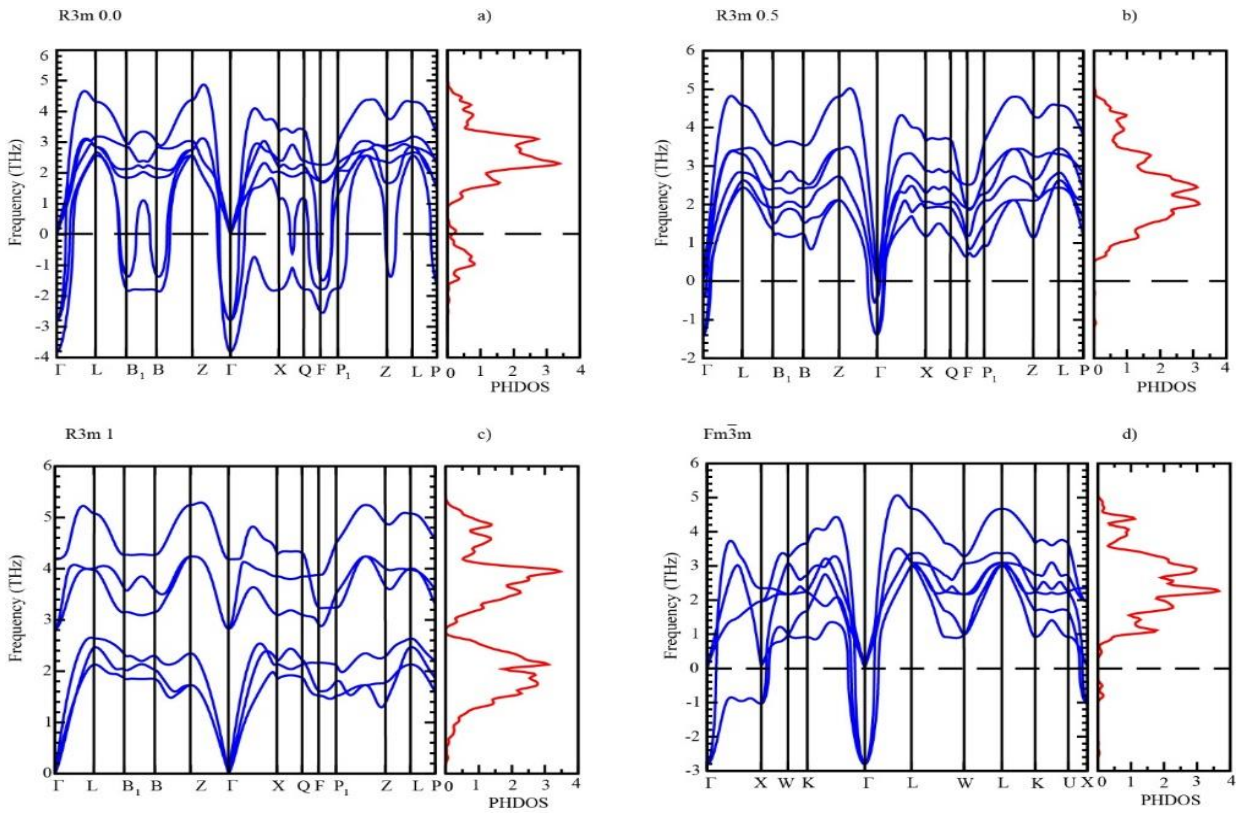

Figure 4.10. Phonon dispersion curves along high-symmetry paths and the phonon density of states (PHDOS) for GeTe of (a) R3m, $\lambda = 0.0$ (b) R3m, $\lambda = 0.5$ (c) R3m, $\lambda = 1$ rhombohedral structure and (d) Fm$\bar{3}$m cubic phase. The negative PHDOS in R3m and with $\lambda = 0.0$, $\lambda = 0.5$ and Fm$\bar{3}$m phase shows instability in GeTe.

Hence, $\mathrm{ZT_e}$ is a more proper descriptor here for the thermoelectric properties when comparing materials with different or no polarization. Figure 4.11 presents the $\mathrm{ZT_e}$ values for the

rhombohedral structure with different levels of polarization in addition to the cubic structure at 300 K and 600 K. From these figures, one can see that ZT_e decreases significantly as the polarization level decreases for $\lambda \leq 1$. However, the change in ZT_e maxima is marginal in the case of $\lambda \geq 1$. Regarding the cubic structure, the ZT_e peaks are comparable to those of the rhombohedral structure at $\lambda = 0.5$. In addition, Figure 4.11 shows that the ZT_e values decrease with increasing the temperature.

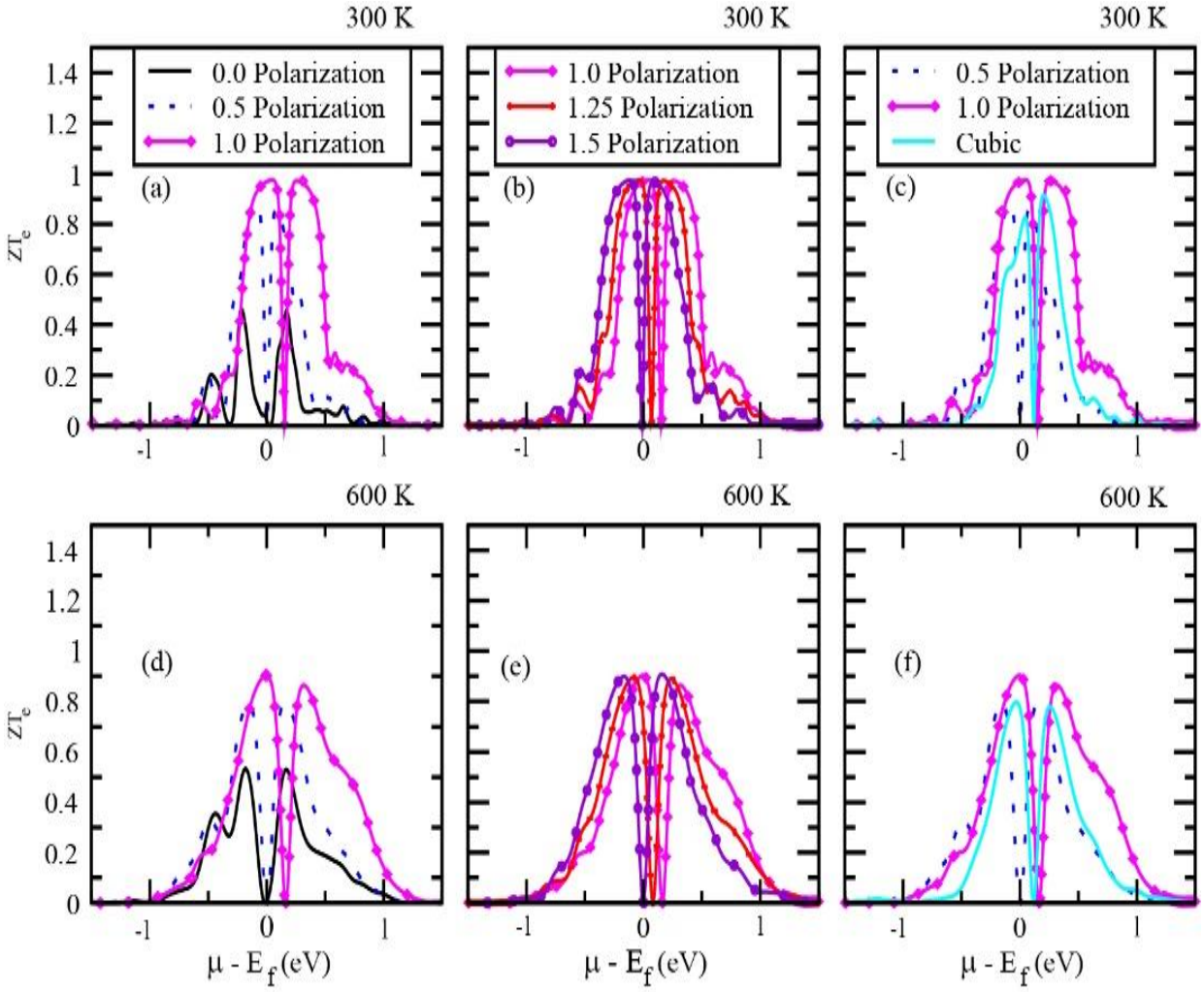

Figure 4.11. ZT_e as a function of the chemical potential deviation from Fermi level in 0.0 polarization, 0.5 polarization, 1.0 polarization, 1.25 polarization, 1.5 polarization and Cubic GeTe in (a, b, c) 300 K, and (d, e, f) 600 K.

Figure 4.12 shows the temperature dependent thermoelectric properties in the temperature range of 50 K to 1000 K for rhombohedral GeTe with different levels of polarization as well as for the cubic structure. Different levels of carrier concentrations were considered ranging from 1×10^{20} to $9 \times 10^{21}\ \mathrm{cm}^{-3}$. For the sake of comparison with previous theoretical and experimental results [46,72], transport properties were calculated at the carrier concentration of $7 \times 10^{20}\ \mathrm{cm}^{-3}$.

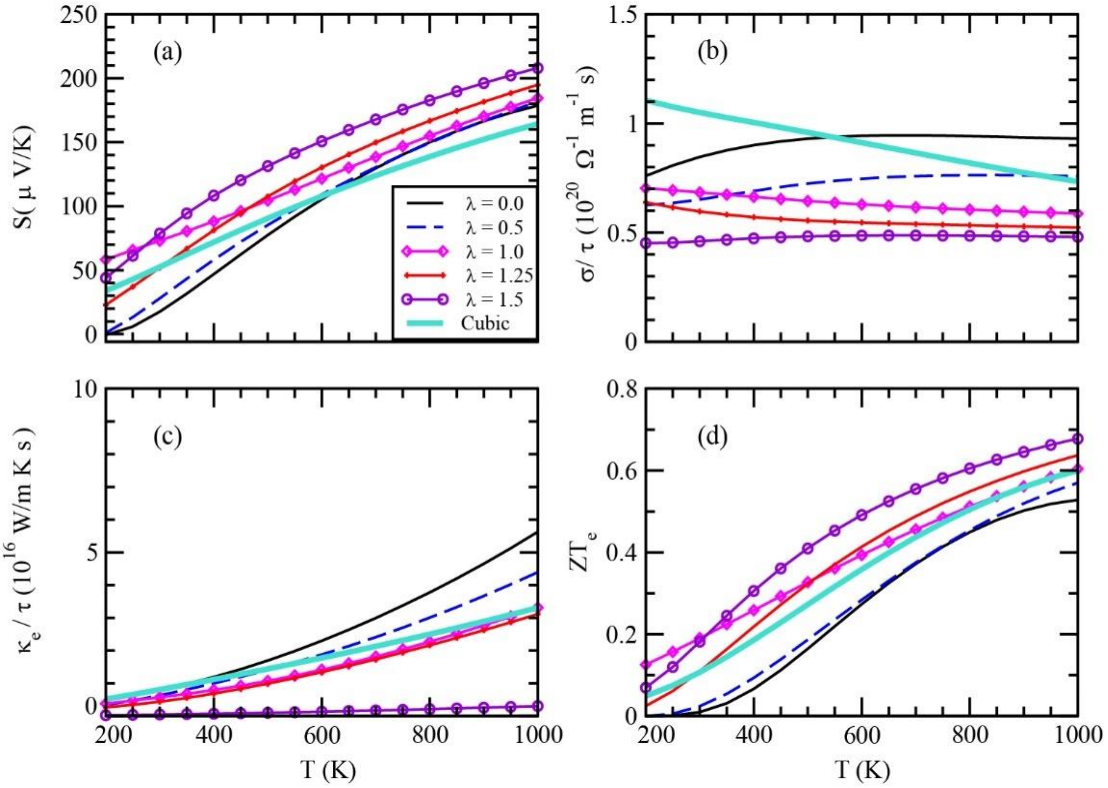

Figure 4.12. Temperature-dependent thermoelectric properties in different levels of polarization and cubic structure: (a) Seebeck coefficient, (b) electrical conductivity in terms of relaxation time, (c) electronic thermal conductivity in terms of relaxation time, and (d) electronic thermoelectric figure of merit.

The calculated Seebeck coefficient at this doping level at 300 K was found to be $73\ \mu\mathrm{V/K}$, which agrees with a previous theoretical work ($68\ \mu\mathrm{V/K}$) [56] and the reported experimental value

($80\ \mu V/K$) [46,72] . Figure 4.12 (a) shows that the rhombohedral polar ground state ($\lambda = 1$) has the highest Seebeck coefficient in the temperature range from 200 K up to around 250 K. It appears that increasing the polarization could increase the Seebeck coefficient at high temperatures (Figure 4.12 (a)), provided one could stabilize such a phase. Indeed, the figure shows that the highest Seebeck coefficient reaches $208\ \mu V/K$ at 1000 K for the rhombohedral structure at $\lambda = 1.5$ (which would be well above the Curie temperature). The cubic structure has smaller Seebeck coefficient values than the rhombohedral ground state at all temperatures. This behavior can be attributed to the lower band gap of the cubic structure than that of the rhombohedral ground state.

Figure 4.12 (b) shows the electrical conductivity within the constant relaxation time approximation as a function of temperature. By increasing the polarization, the conductivity decreases. By increasing the temperature, the conductivity decreases to less than 0.5 $\times 10^{20}\Omega^{-1}\mathrm{m}^{-1}s$ for cubic and rhombohedral GeTe with polarization states $\lambda \geq 1$. However, the electrical conductivity shows a constant behavior at most temperatures only for $\lambda = 1.5$ for the rhombohedral structure.

Figure 4.12 (c) shows a nonlinear increase in the electronic thermal conductivity κ_e/τ as a function of temperature for different polarization levels. Figure 4.12 (d) shows a subsequent increase in ZT_e as the polarization level increases. The rhombohedral structure shows higher ZT_e values than the cubic structure even at temperatures higher than the transition temperature. The polar structure at $\lambda = 1.5$ shows higher ZT_e values than the cubic structure at high temperatures. Therefore, it becomes clear that by stabilizing a structure with a large polarization at high temperatures would be desirable to obtain more efficient TE materials. Potential pathways towards that would be to use solid solutions with a high Curie temperature polar material or use strain engineering. In the latter case, growing epitaxial films that bi-axially compress the directions

perpendicular to the polar axis may help to tune the Curie temperature of GeTe in order to achieve high TE performances.

In order to investigate the stability and electron-phonon interaction, the lattice dynamics of this material should be investigated. In Figure 4.13, the phonon dispersion relation and dynamical stability are depicted for two polarization levels of the rhombohedral structure, namely 1.5 and 1.

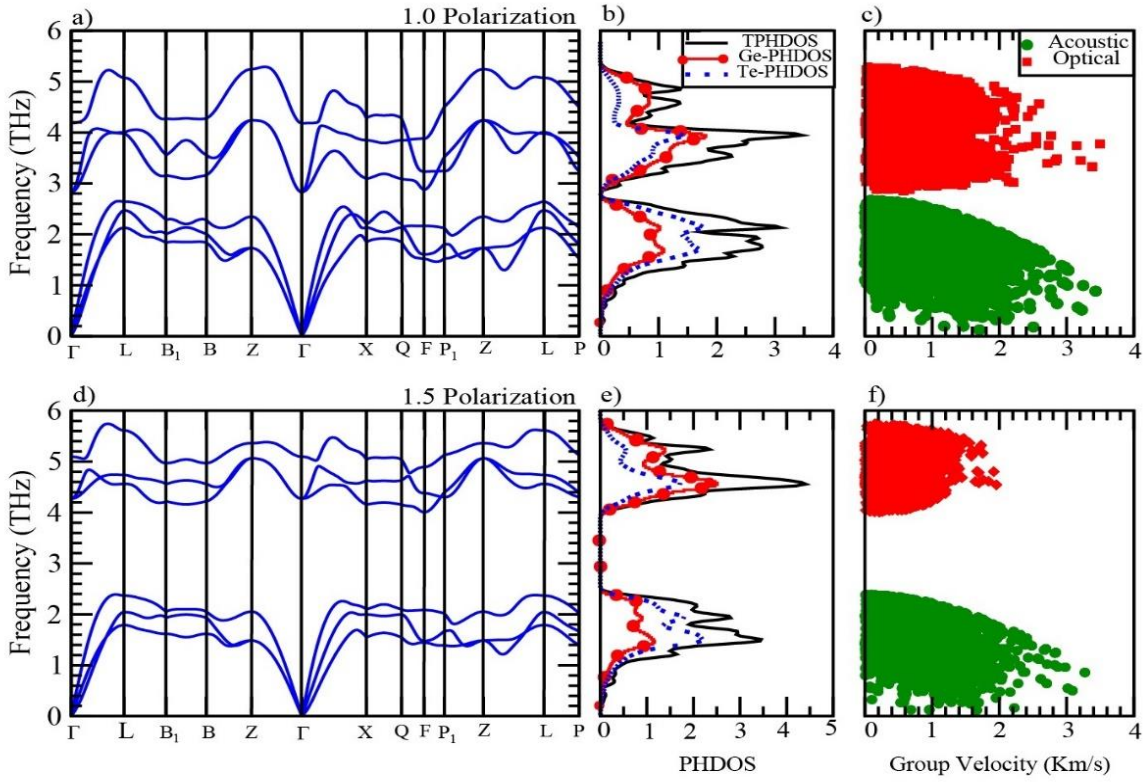

Figure 4.13.(a)(d) Calculated phonon dispersion relation along high-symmetry points, (b) (e) phonon density of states and (c) (f) group velocity for GeTe with polarization $\lambda = 1$(top panel) $\lambda = 1.5$ (bottom panel).

The phonon dispersion relation for rhombohedral GeTe with $\lambda = 0, 0.5$ and cubic GeTe was shown in Figure 4.10. As seen in Figure 4.13, both polarization states $\lambda = 1$ and $\lambda = 1.5$ are

dynamically stable as neither exhibits any imaginary frequency mode across the whole Brillouin zone. While insignificant changes are observed for the acoustic modes between the polarization states $\lambda = 1$ and $\lambda = 1.5$, the frequency gap between acoustic and optical branches widens upon increasing the polarization (Figure 4.13). By checking Figure 4.13 (c) and (f), it seems that both acoustic modes and optical modes play a role in lattice thermal conductivity, but mostly acoustic and by increasing the polarization, the role of the optical mode decreases.

The equation that clarifies the relation between group velocity and the lattice thermal conductivity is:

$$\kappa_l^{\alpha\beta} = \frac{1}{NVk_BT^2}\sum_{\lambda} n_\lambda^0(n_\lambda^0+1)(\hbar\omega_\lambda)^2 v_\lambda^\alpha v_\lambda^\beta \frac{dk}{(2\pi)^3}\tau_\lambda \,, \qquad \text{(Equation 4.8)}$$

where k_B, V, and N are the Boltzmann constant, volume of unit cell, and the total number of phonon wave vectors included in the summation. In this formula, n_λ^0 denotes the equilibrium occupation probability for phonons. The role of frequency and group velocity by the phonon mode of λ is defined by ω_λ and v_λ, respectively, with Cartesian coordinates indexed by α and β. As can be deduced from the formula and Figure 4.13 (c) and (f), the lattice thermal conductivity can increase due to increased frequency of optical mode [73].

The temperature dependent lattice thermal conductivity of rhombohedral GeTe with polarization 1 and 1.5 is calculated and the result is provided in Figure 4.14 (a). It can be deduced from the figure that the lattice thermal conductivity increases by increasing the polar distortion, which increases the frequency gap between the optical and acoustic modes. This plot clarifies that the acoustic modes play an important role in the value of the lattice thermal conductivity of this material. The calculated κ_{latt} of the rhombohedral GeTe at 300 K with polarization 1 is 2.64 $\mathrm{W/mK}$ in agreement with previous results [74]. However, it increases to 7.85 $\mathrm{W/mK}$ for the higher polarization (1.5).

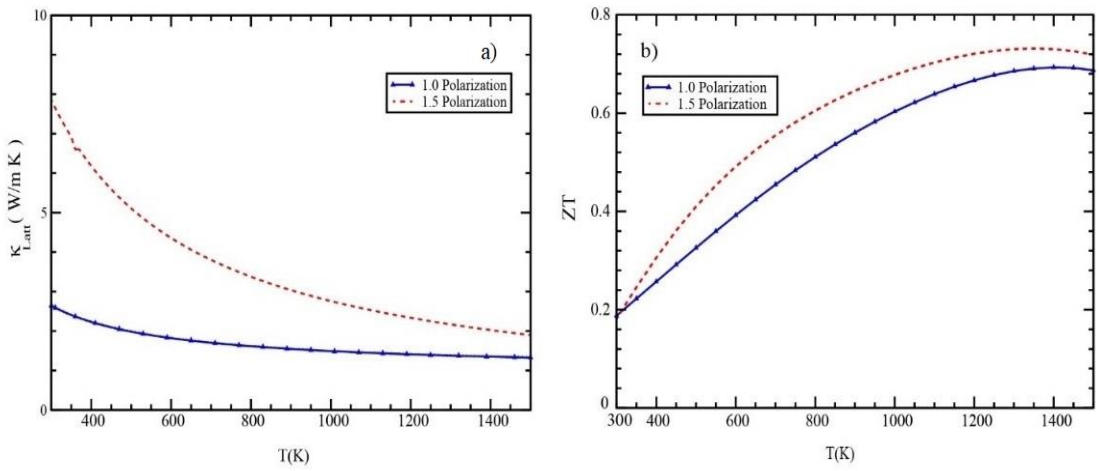

Figure 4.14. (a) The lattice thermal conductivity (κ_{latt}), and (b) temperature dependent figure of merit (ZT) in polarization 1 (dotted line), and 1.5 (dashed line).

The thermoelectric figure of merit, ZT, is calculated using a relaxation time of $\tau = 10^{-14}$s which is a common value for similar calculation [23,39] and the result is shown in Figure 4.14 (b). The maximum values of ZT at the polarization levels of 1.5 and 1 are 0.73 and 0.69 at 1350 K, respectively. The ZT value at λ = 1 is in good agreement with previous results [23].

4.4. Summary

The structural electronic, and thermoelectric properties of rhombohedral GeTe with different levels of polarization and Cubic GeTe were investigated using density functional theory combined with Boltzmann transport theory. The rhombohedral structure at $\lambda = 1$ is the ground state structure, which has an indirect band gap of 0.55 eV, while the cubic structure has a direct band gap of 0.35 eV. The rhombohedral structure shows a better thermoelectric behavior at high polarization levels than the cubic phase even at temperatures above transition temperatures. This can be attributed to the presence of ferroelectricity in the rhombohedral structure of GeTe. The thermoelectric properties of material were improved at a high polarization level of 1.5, while the

band gap remained about the same. This indicates that stabilizing large polarization at high temperatures in polar thermoelectric materials may help to enhance their thermoelectric properties.

Chapter 5: Effect of Doping on the Thermoelectric Properties of Bulk GeS and GeSe Chalcogenides

5.1 Introduction

Materials with similar structures to SnSe that have a high figure-of-merit ($ZT > 1$) have attracted a lot of attention [75-77]. Accordingly, GeS and GeSe alloys have been studied from different aspects, but there is still a room for improvement of the thermoelectric properties of these materials. For example, the transport properties of bulk SnSe, SnS, GeS, and GeSe have been studied comprehensively and the phonon dispersion relations of these structures have been provided by Ding et al. [63]. In addition, the thermoelectric properties of IV-VI two-dimensional groups were studied in order to attempt to enhance the energy storage in two-dimensional materials [78]. Furthermore, the lattice thermal conductivity of two-dimensional SnSe, SnS, GeS, and GeSe were investigated and reported by Shafique et al. and Morales et al. [79,80]. The effects of hole-doped GeSe were studied both experimentally and computationally, which have shown an increase in the quality of transport properties in these materials [81,82]. Recently, a study by Yuan et al reported the effect of hydrostatic pressure on orthorhombic GeSe and the anisotropic lattice thermal conductivity.[48]. In most of the reports, the lattice thermal conductivity of bulk GeS and GeSe is neglected due to the time consuming and expensive calculations [83]. This study presents the electronic and thermoelectric properties of GeS and GeSe mono-chalcogenides and their doped structures with different elements of group III, IV, and IV. Finally, the lattice thermal conductivity of doped and non-doped material for the sake of comparison using the Slack equation is calculated to find the effect of doping on lattice thermal conductivity.

5.2 Computation Methodology

The structural, electronic, and thermoelectric properties of orthorhombic GeS and GeSe

are calculated based on first principle calculation using Kohn-Sham density functional theory and Boltzmann transport theory. The structures were optimized, and electron energy calculated using Vienna ab initio simulation (VASP). The exchange correlation function was treated using the generalized gradient approximation (GGA) in the form of Perdew–Burke–Ernzerhof (PBE). The kinetic cut off energy of plane waves was set to 520 eV. In order increase the accuracy of calculations, lattice parameters were optimized through a relaxation step with the force convergence and energy convergence criteria of 1×10^{-2} eV/Å and 1×10^{-6} eV, respectively. The self-consistency calculations for the first Brilllouin zone (BZ) with a k-mesh of $24 \times 20 \times 8$ was performed with optimized lattice parameters in both GeS and GeSe structure. The effect of spin-orbit could be neglected due to its negligible effect on the total energy results. The non-self-consistent calculations were repeated using a denser k mesh of $120 \times 100 \times 40$ in GeS and GeSe to calculate the thermoelectric properties of these materials. The Boltzmann transport theory was used to calculate the transport coefficient based on the electronic structure using Boltztrap code [59]. The Slack equation was used to calculate lattice thermal conductivity of these materials.

5.3 Results and Discussion

This section presents structural, electronic, and transport properties of the orthorhombic GeS and Gese alloys. The effect of doping with different elements in these materials is investigated and the best doped material for further investigations is introduced.

5.3.1 GeS and GeSe Structure

At room temperature both GeS and GeSe have orthorhombic crystal structure ($a \neq b \neq c$) with space group of Pnma (#62). The unit cell of these chalcogenides consists of two layers, where

the thickness of each layer is two atoms that are stacked together along the c-axis by van der Waals interaction. In each layer, each atom is bonded to three nearest neighbors through covalent bonding that forms a zigzag chain along the a-axis and armchair chain along the b-axis (see Fig 5.1(a)-(d)).

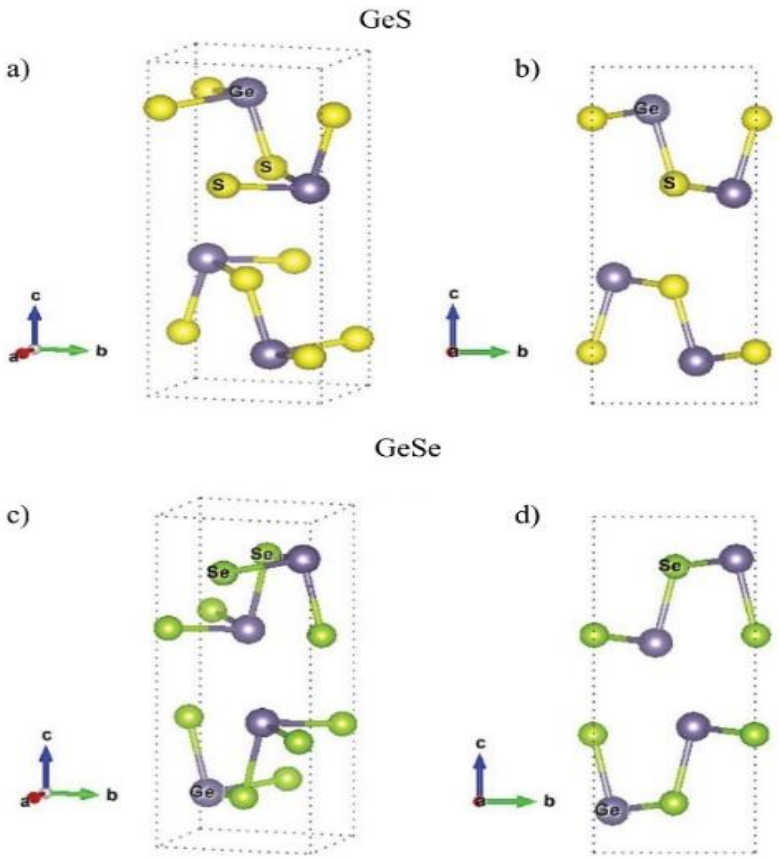

Figure 5.1. The crystal structure of (a) (b) GeS and (c) (d) GeSe in orthorhombic phase (Ge purple spheres S(Se) yellow(green) spheres).

The calculated lattice parameters for the ground state orthorhombic GeS and GeSe are: $a_{GeS} = 3.67$ Å , $b_{GeS} = 4.43$ Å , $c_{GeS} = 10.76$ Å, $a_{GeSe} = 3.89$ Å , $b_{GeSe} = 4.51$ Å, and $c_{GeSe} = 11.16$ Å, respectively(see Table 5.1). From Table 5.1, one can see that the calculated lattice parameter of these alloys agrees with previous DFT calculations within a percentage difference of 1-3% [69,84,85].

Table 5.1. The theoretical and experimental structural parameters of GeS and GeSe.

Parameter	a (Å)	b (Å)	c (Å)	E_g (eV) GGA
GeS				
Other Works	3.51[a], 3.67[c]	4.29[a], 4.30[c]	10.42[a], 10.47	1.25[a]-1.6[b]
Present work	3.67	4.43	10.77	1.23
GeSe				
Other Works	3.83[a], 3.85[d]	4.38[a], 4.40[d]	10.82[a, d]	0.87[a], 1.07[c]
Present work	3.89	4.51	11.16	0.82

[a]Ref [69],[b]Ref [86], [c]Ref [84], [d]Ref[85]

5.3.2 Electronic Properties

The energy band structures of GeS and GeSe are shown in Figure 5.2. Here, the high symmetry points are Γ, Z, U, X , Y, S, and R at the k-points $(0,0,0)$, $(0,0,1/2)$, $(1/2,0,1/2)$, $(1/2,0,0)$, $(0,1/2,0)$, and $(1/2,1/2,0)$, respectively. The band gap is determined as the difference between valence band maximum (VBM) and conduction band minimum (CBM).

The figure provides the VBM for GeS located at 0.81 eV below the Fermi level around the Γ point and the CBM located at the same point along with 0.42 eV on top of the Fermi level. As a result, the band gap for GeS is direct with the value of 1.23 eV. The VBM for GeSe located at 0.39 eV below the fermi level at $\sum$ point and the CBM at 0.43 eV on top of the Fermi level at around Γ point, so the band gap for GeSe is indirect with the value of 0.82 eV.

The percentage difference of calculated band gap of GeS and GeSe and other experimental reports for GeS is 20% and for GeSe is 23% [84, 86]. However, this value is negligible when the results are compared with other DFT calculations [69].

The total density of states (TDOS) and the projected density of states (PDOS) of GeS and

GeSe are presented in Fig. 5.3. The zero point in the x-axis is equal to the energy of the Fermi level. The main contribution of the density of states is due to hybridization of the p-orbitals of Ge with those of S and Se. The p-orbitals of S and Se are dominate the valence bands, while the conduction bands are dominated by the p-orbital of Ge. The effects of s-bands in all Ge, S, and Se are not critical because both are far from the Fermi level.

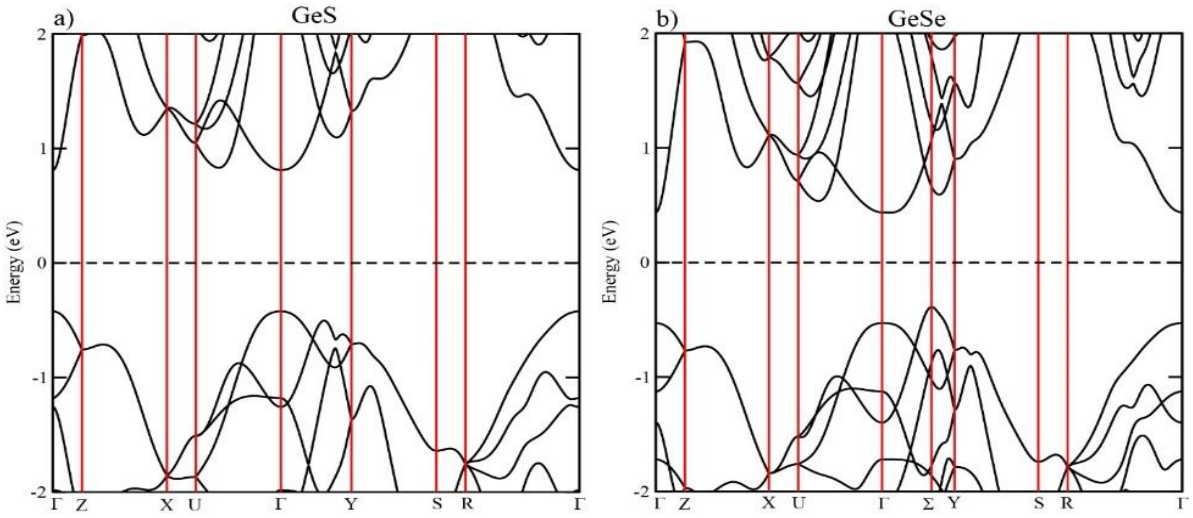

Figure 5.2. (a) The band structures of GeS and (b) GeSe alloys.

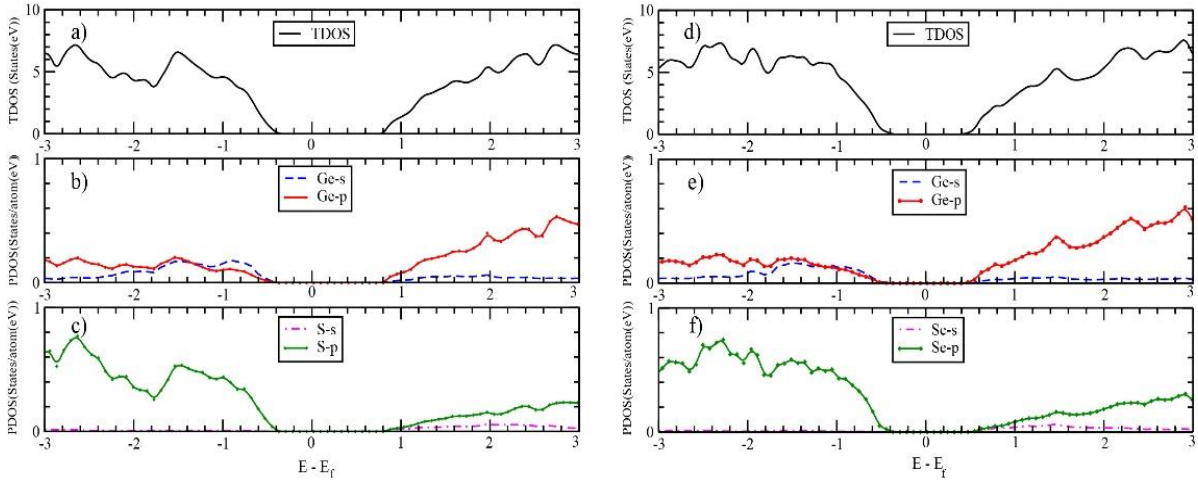

Figure 5.3. Total density of states (a), (d) and projected density of states (b), (c), (e), and (f) of GeS (left panel) and GeSe (right panel).

5.3.3 GeS and GeSe Doping

Doping has proved to be an effective way of modifying a material in order to investigate the thermoelectric properties of many materials, some examples of this are SnSe and Mg_2Si [87,88]. For the purpose of this study, GeS and GeSe were doped by X = Al, As, Bi, In, Pb, Sb, Se, S, Si, Sn and Te once at the Ge site and another at the chalcogens site (S/Se). To determine which dopant to proceed with, the power factors of these alloys (variants $GeS_{0.75}X_{0.25}$, $Ge_{0.75}X_{0.25}S$, $GeSe_{0.75}X_{0.25}$, and $Ge_{0.75}X_{0.25}Se$) were calculated at 600 K. This was then taken into consideration for selecting a dopant element that positively affects the thermoelectric properties of GeS and GeSe (see Figure 5.4). As shown in Fig. 5.4, the highest power factor was plotted as a function of energy and was obtained by doping S in Ge site and doping Te in Se site of GeSe. In follow up to these results, the calculations were considered for different dopant concentrations on GeSe, namely $Ge_{(1-x)}S_xSe_{(1-x)}Te_x$ (x = 0.0, 0.25, 0.5, 0.75) doped alloys as presented in this sub-section.

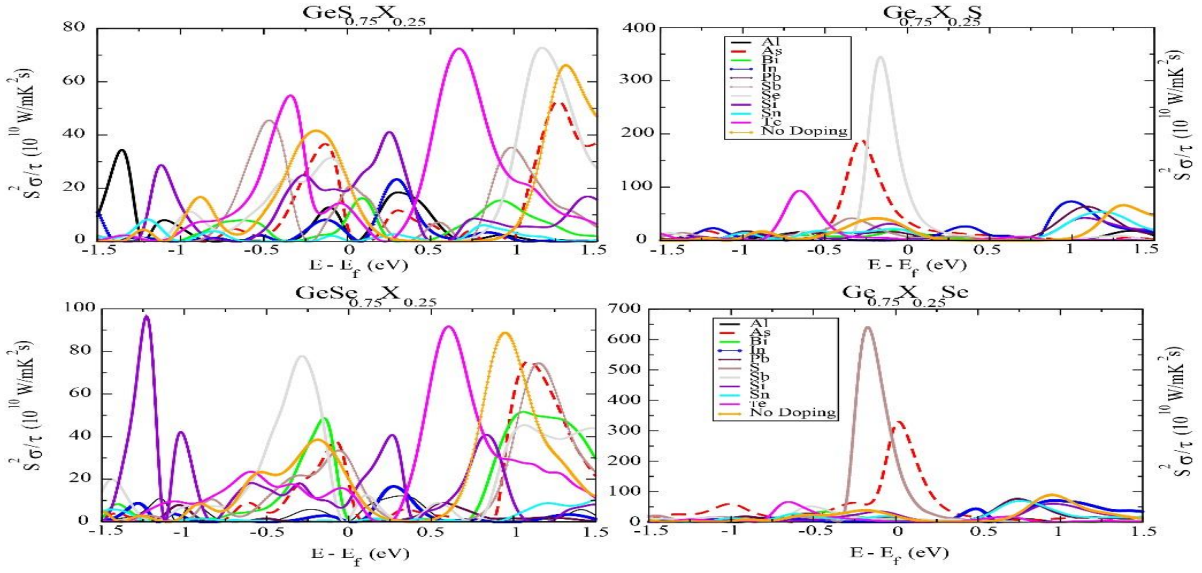

Figure 5.4. Power factor of GeS $_{0.75}$X $_{0.25}$, Ge $_{0.75}$X $_{0.25}$S, GeSe $_{0.75}$X $_{0.25}$, and Ge $_{0.75}$X $_{0.25}$Se alloys.

Structural Stability

The structural properties of $Ge_{(1-x)}S_xSe_{(1-x)}Te_x$ (x=0.0, 0.25, 0.5, 0.75) alloys are presented here. By adding impurities to the orthorhombic GeSe, it converts to a monoclinic structure (see Figure 5.5). The presence of these impurities in the structure of the material changes the angles of the unit cell and even the lattice constants (see Table 5.2).

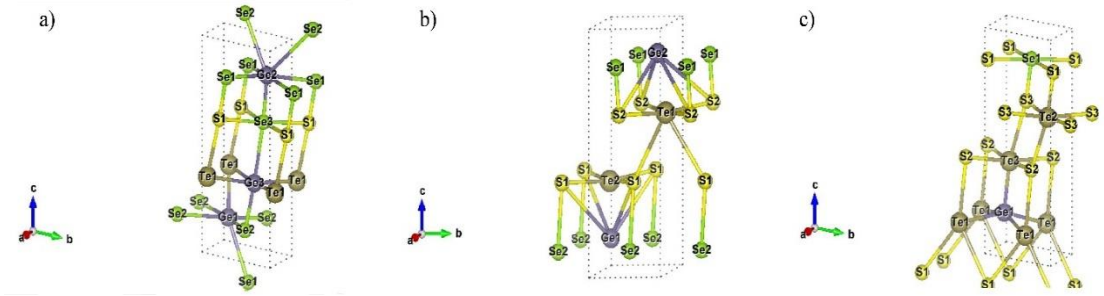

Figure 5.5. The unit cell of (a) $Ge_{0.75}S_{0.25}Se_{0.75}Te_{0.25}$ (b) $Ge_{0.50}S_{0.50}Se_{0.50}Te_{0.50}$, and (c) $Ge_{0.25}S_{0.75}Se_{0.25}Te_{0.75}$ alloys.

Table 5.2. Calculated lattice parameters of $Ge_{0.75}\,S_{0.25}\,Se_{0.75}Te_{0.25}$, $Ge_{0.50}\,S_{0.50}\,Se_{0.50}Te_{0.50}$, and $Ge_{0.25}\,S_{0.75}\,Se_{0.25}Te_{0.75}$ alloys.

Doping level	a (Å)	b (Å)	c (Å)	α	β	γ	Unit Cell
$Ge_{0.75}\,S_{0.25}\,Se_{0.75}Te_{0.25}$	4.063	4.249	11.485	98.574	90	90	Monoclinic
$Ge_{0.50}\,S_{0.50}\,Se_{0.50}Te_{0.50}$	3.882	4.137	12.231	98.5748	90	90	Monoclinic
$Ge_{0.25}\,S_{0.75}\,Se_{0.25}Te_{0.75}$	4.009	4.105	11.989	96.4600	90	89.999	Monoclinic

The stability of the structure can be examined by calculating the elastic constants. The elastic constant matrix for the considered structures is a 6×6 matrix. The crystal structure is considered to be stable in the case of the monoclinic crystal if all the eigen values of the elastic constant matrix are positive [89]. The calculated elastic constants of aforementioned structures are

provided in Table 5. 3.

Table 5.3. Elastic constants $C_{ij}(GPa)$ of $Ge_{0.75}S_{0.25}Se_{0.75}Te_{0.25}$, $Ge_{0.50}S_{0.50}Se_{0.50}Te_{0.50}$, and $Ge_{0.25}S_{0.75}Se_{0.25}Te_{0.75}$ alloys.

Doping level	C_{11}	C_{12}	C_{13}	C_{22}	C_{33}	C_{44}	C_{55}	C_{66}
$Ge_{0.75}S_{0.25}Se_{0.75}Te_{0.25}$	79.80	34.49	0.85	43.94	48.67	6.03	4.03	29.78
$Ge_{0.50}S_{0.50}Se_{0.50}Te_{0.50}$	96.88	61.81	0.56	76.13	47.46	9.81	-4.34	34.87
$Ge_{0.25}S_{0.75}Se_{0.25}Te_{0.75}$	89.63	75.28	2.15	92.79	66.78	4.20	2.86	10.84
GeSe	84.64	34.915	13.022	29.164	63.802	15.632	17.156	35.504]

Among all the aforementioned structures, the only structure that is not stable is $Ge_{0.50}$ $S_{0.50}$ $Se_{0.50}Te_{0.50}$, since it has negative eigen value among all eigen values (see Table 5.4). The other structures can be considered stable.

Table 5.4. Eigen values of elastic constant matrix of $Ge_{0.75}$ $S_{0.25}$ $Se_{0.75}Te_{0.25}$, $Ge_{0.50}$ $S_{0.50}$ $Se_{0.50}Te_{0.50}$, $Ge_{0.25}$ $S_{0.75}$ $Se_{0.25}Te_{0.75}$, and GeSe alloys.

Doping level	λ_1	λ_2	λ_3	λ_4	λ_5	λ_6
$Ge_{0.75}S_{0.25}Se_{0.75}Te_{0.25}$	101.198	49.22	22.802	5.225	3.947	29.872
$Ge_{0.50}S_{0.50}Se_{0.50}Te_{0.50}$	149.564	48.937	22.325	9.46	-5.27	35.80
$Ge_{0.25}S_{0.75}Se_{0.25}Te_{0.75}$	167.16	66.718	16.033	11.353	3.49	2.36
GeSe	108.14	11.694	57.771	15.632	17.156	35.504

There are some other constants such as the bulk modulus B, and shear modulus G that should be addressed to be used in the process of determining lattice thermal conductivity.

$$B = (C_{11} + 2C_{12})/3 \quad \text{(Equation 5.1)}$$

$$G = (G_V + G_R)/2 \quad \text{(Equation 5.2)}$$

$$G_V = (C_{11} - C_{12} + 3C_{44})/5, \quad \text{(Equation 5.3)}$$

$$G_R = (5C_{44}(C_{11} - C_{12}))/4C_{44} + (C_{11} - C_{12}), \quad \text{(Equation 5.4)}$$

These parameters will be used later for calculating lattice thermal conductivity through the Slack equation. Here, the bulk modulus B and shear modulus, G, of $Ge_{0.75}S_{0.25}Se_{0.75}Te_{0.25}$, $Ge_{0.25}S_{0.75}Se_{0.25}Te_{0.75}$, and GeSe are provided in Table 5. 5, since they are more stable in comparison to $Ge_{0.50}S_{0.50}Se_{0.50}Te_{0.50}$.

Table 5.5. Bulk modulus B and shear modulus G of $Ge_{0.75}S_{0.25}Se_{0.75}Te_{0.25}$, $Ge_{0.25}S_{0.75}Se_{0.25}Te_{0.75}$, and GeSe alloys.

Doping level	B	G	G_V	G_R
$Ge_{0.75}S_{0.25}Se_{0.75}Te_{0.25}$	74.39	57.31	12.68	101.95
$Ge_{0.25}S_{0.75}Se_{0.25}Te_{0.75}$	120.09	18.84	5.39	32.29
GeSe	77.23	65.60	19.32	111.88

Band Structure of Doped alloys

The band gap of the crystal structure is changed by introducing dopants to a parent crystal. Depending on whether the added impurities are electron donors or acceptors, new energy levels can be added to the conduction band or valence band [90]. Since Te and S are both from group VI and they have six electrons in their valence band, both of them are considered as electron donors, so some degeneracy should be seen in the conduction band (see Figure 5.6). Dopants can also shift the energy bands relative to the Fermi level. As can be inferred from Figure 5.6, introducing different concentrations of Te to GeSe resulted in the decrease of the band gap energy. The band

gap of GeSe (0.82 eV) decreases to 0.62 eV in $GeSe_{0.25}Te_{0.25}$ and reaches 0.42 eV in $GeSe_{0.50}Te_{0.50}$ and $GeSe_{0.25}Te_{0.75}$. The figure clarifies that the band gaps of $GeSe_{0.75}Te_{0.25}$ and $GeSe_{0.25}Te_{0.75}$ are indirect, while that of $GeSe_{0.50}Te_{0.50}$ is direct.

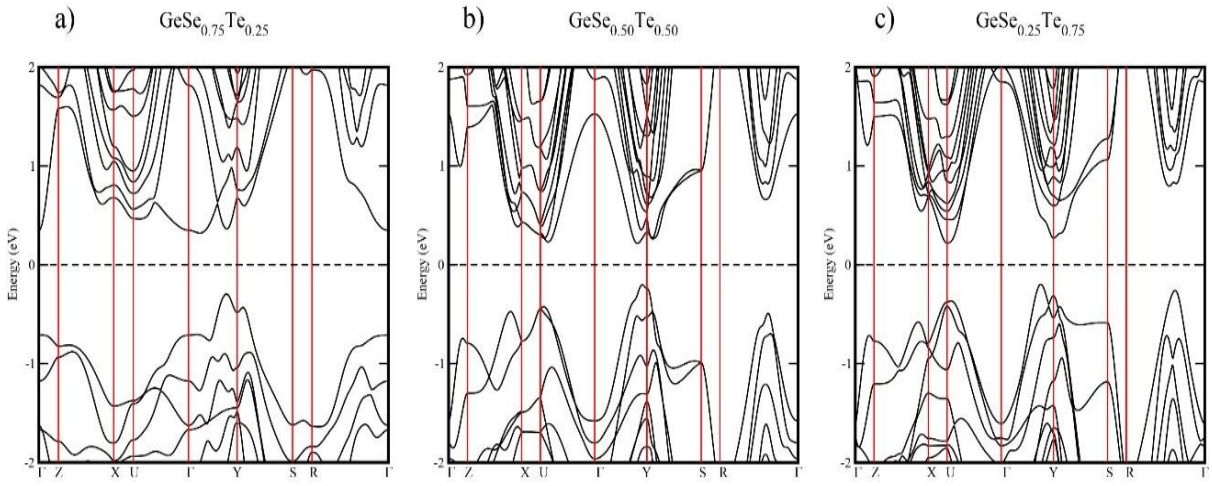

Figure 5.6. Electronic band structure of (a) $GeSe_{0.25}Te_{0.25}$, (b) $GeSe_{0.50}Te_{0.50}$, and (c) $GeSe_{0.25}Te_{0.75}$ alloys.

Adding S as dopant to the Ge site of GeSe, not only increases the degeneracy but also causes band bending around the Fermi level. Doping GeSe with S at the Ge site converts the material to a metal, which means the band gap in $Ge_{(1-x)}S_xSe$ (x=0.25,0.50, 0.75) decreases to zero. The effect of adding different concentrations of S to GeSe on band structure is elaborated in Figure 5.7.

Finally, by adding S on Ge site and adding Te on Se site with different concentration in GeSe led to the combination of aforementioned effects, see Figure 5.8. The number of degenerate states in the valence band increases and the band gap decreases to zero, so the material shows a metallic behavior. As a result, the electrical conductivity of $Ge_{(1-x)}S_xSe_{(1-x)}Te_x$ (x=0.0, 0.25, 0.5, 0.75) should be higher in comparison to GeSe.

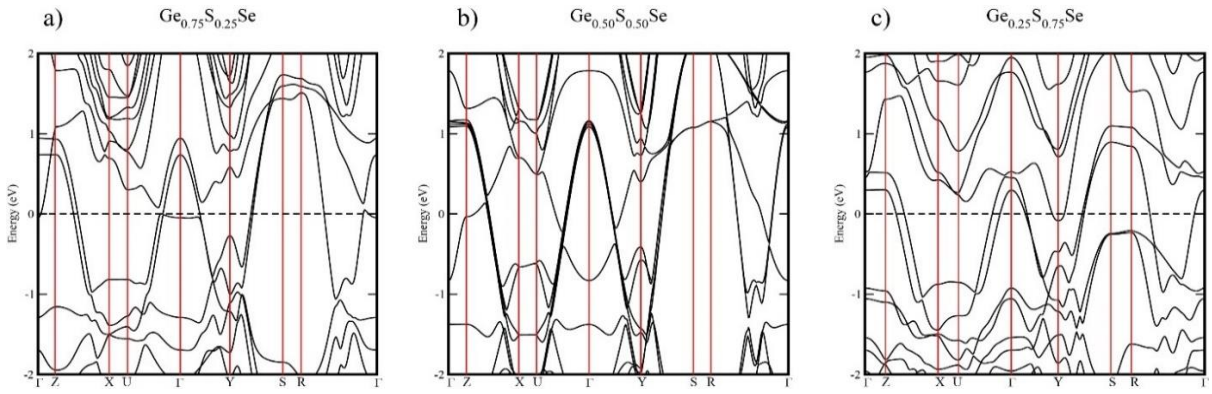

Figure 5.7. Electronic band structure of (a) $Ge_{0.75}S_{0.25}Se$, (b) $Ge_{0.5}S_{0.5}Se$, and (c) $Ge_{0.25}S_{0.75}Se$ alloys.

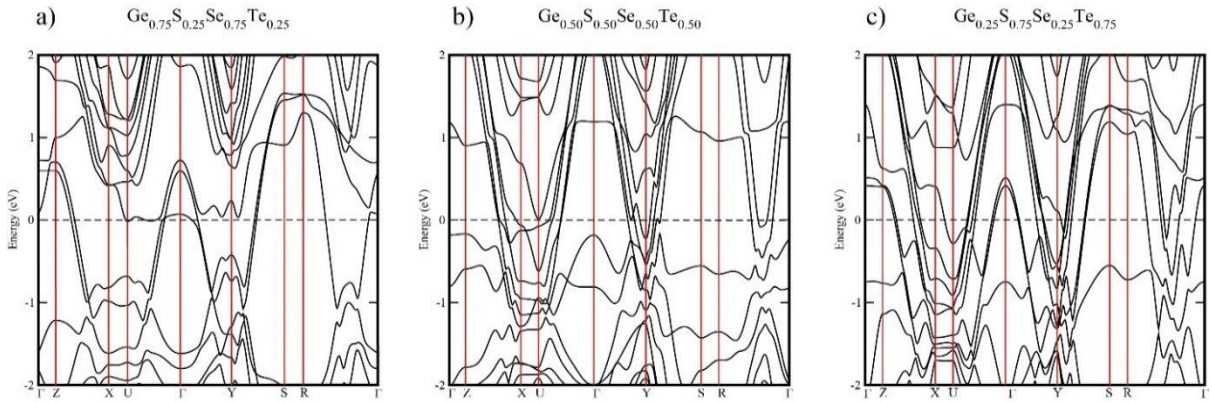

Figure 5.8. Electronic band structure of (a) $Ge_{0.75}S_{0.25}Se_{0.75}Te_{0.25}$, (b) $Ge_{0.50}S_{0.50}Se_{0.50}Te_{0.50}$, and (c) $Ge_{0.75}S_{0.25}Se_{0.75}Te_{0.25}$ alloys.

Transport Properties

The transport properties of $Ge_{(1-x)}S_xSe_{(1-x)}Te_x$ (x=0.0, 0.25, 0.5, 0.75) as a function of energy for both 300 K and 600 K are shown in Figure 5.9. The Seebeck coefficient is found to decrease drastically, almost to the point of a plateau by introducing dopants to the material (see Figure 5. 9 (a)). It is also found that the Seebeck coefficient decreases by increasing temperature in line with the aforementioned inverse relationship with temperature. The electrical conductivity is also depicted in Figure 5.9 (b). As was predicted previously, increasing the impurity level in

GeSe results in a higher electrical conductivity, which cannot be affected noticeably by temperature. In addition, the power factor $S^2\sigma/\tau$ plotted in Fig. 5.9 (c) shows that the highest power factor is obtained for the case of $Ge_{0.75}S_{0.25}Se_{0.75}Te_{0.25}$ (black thick line). The power factor was found to increase from 158 10^{10} W/mK^2s at 300 K to 480 10^{10} W/mK^2s at 600 K.

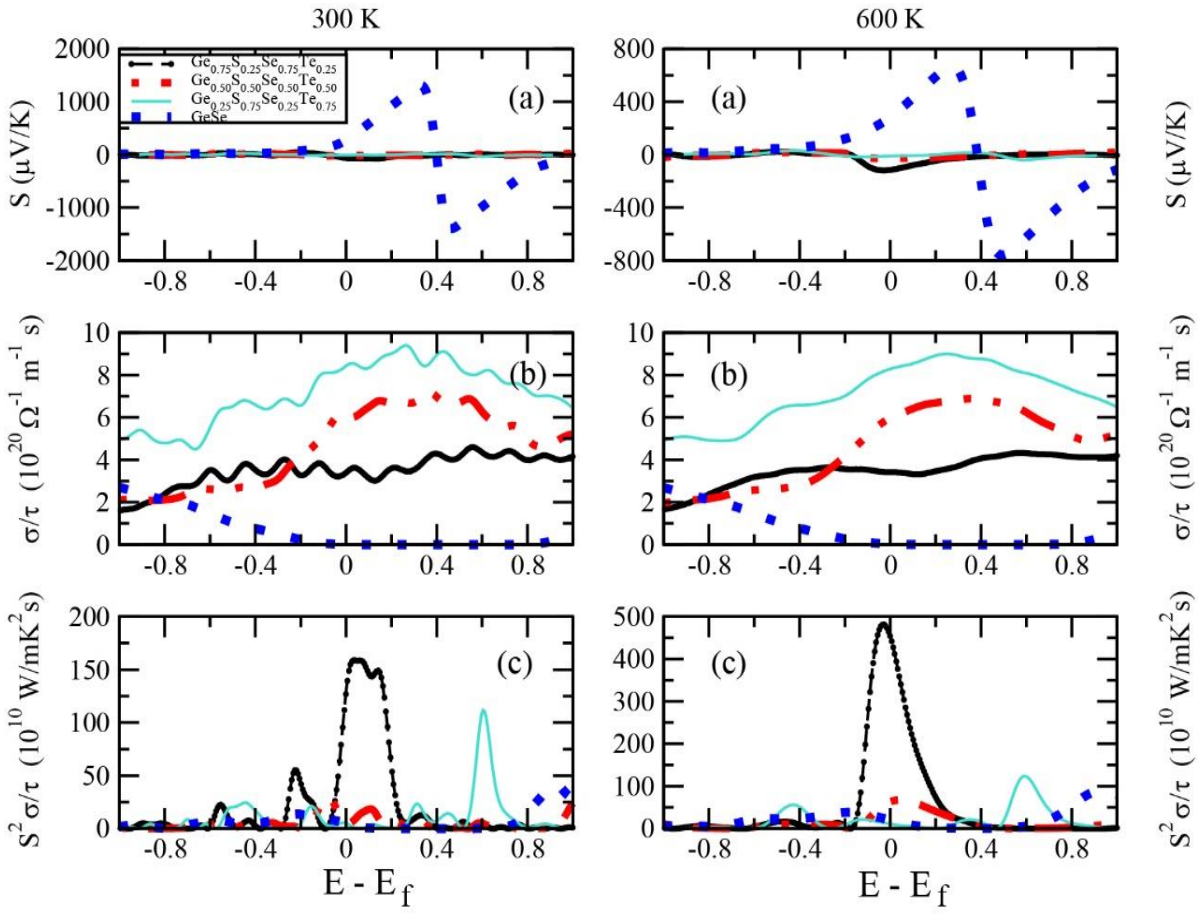

Figure 5.9. Transport properties of GeSe, $Ge_{0.75}S_{0.25}Se_{0.75}Te_{0.25}$, $Ge_{0.50}S_{0.50}Se_{0.50}Te_{0.50}$, $Ge_{0.25}S_{0.75}Se_{0.25}Te_{0.75}$, at 300 K (left panel) and 600 K (right panel). (a) Seebeck, (b) electrical conductivity, and (c) power factor.

Lattice Thermal conductivity

The lattice thermal conductivity is an essential quantity to evaluate the figure of merit of the materials using the Slack equation [91], which has been extensively used in some studies [92-

94]. This method assumes that the acoustic modes are responsible for the heat transfer, which is expressed as follows:

$$\kappa_l = \frac{2.43 \times 10^{-6}}{1 - 0.514\gamma^{-1} + 0.228\gamma^{-2}} \frac{M_{av}\theta_D^3 V^{1/3}}{\gamma^2 n^{2/3} T}. \quad \text{(Equation 5.5)}$$

Here M_{av} is the average atomic mass of n atoms in the unit cell, θ_D^3 is the Debye temperature, V is the volume per atom, γ the Grüneisen parameter, and T is the temperature.

The Grüneisen parameter in the form of formula is defined as follows:

$$\gamma = \frac{9 - 12(v_t/v_l)^2}{2 + 4(v_t/v_l)^2}, \quad \text{(Equation 5.6)}$$

where v_t and v_l are transversal and longitudinal velocities.

The equation of the Debye temperature is expressed as follows:

$$\theta_D = \frac{h}{k_B}\left(\frac{3n}{4\pi\Omega}\right)^{1/3} v_a, \quad \text{(Equation 5.7)}$$

where v_t, v_l, and v_a are defined as:

$$v_t = \sqrt{\frac{G}{\rho}}, \quad \text{(Equation 5.8)}$$

$$v_l = \sqrt{\frac{B + 4G/3}{\rho}}, \quad \text{(Equation 5.9)}$$

$$v_a = \left[\frac{1}{3}\left(\frac{2}{v_t^3} + \frac{1}{v_l^3}\right)\right]^{-1/3} \quad \text{(Equation 5.10)}$$

where ρ is the mass density. The shear modulus (G) and bulk modulus (B) were provided in Equations 5.1 and 5.3, and values were mentioned in Table 5.5.

The calculated Debye temperature for GeSe was found to be 212 K, which agrees with a previous reported value of 214 K [95]. The calculated κ_{Lat} was 1.78 W/mK at 300 K, which is in

excellent agreement with the reported experimental value of about 1.8 W/mK at 300 K [96]. The κ_{Lat} of $Ge_{0.75}S_{0.25}Se_{0.75}Te_{0.25}$ decreases to the value of 0.74 W/mK at 300 K.

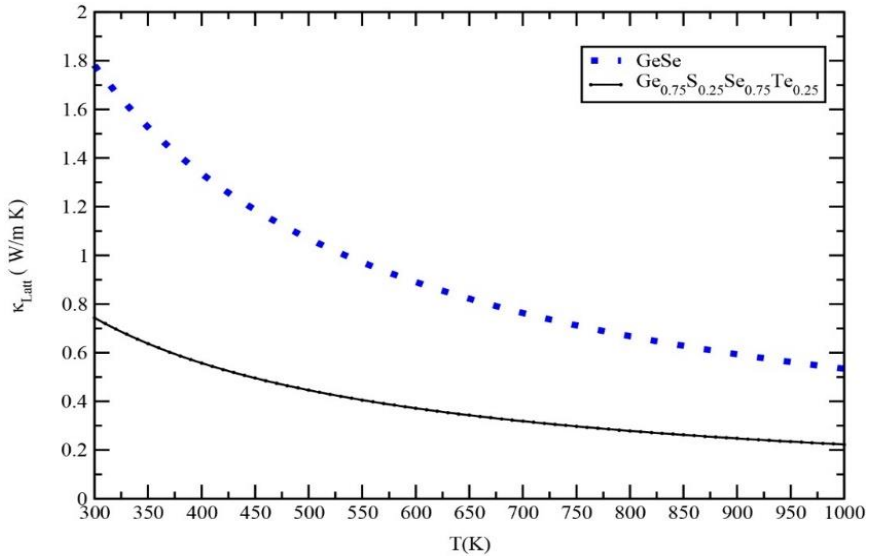

Figure 5.10. Lattice thermal conductivity of GeSe (dashed line) and $Ge_{0.75}S_{0.25}Se_{0.75}Te_{0.25}$ (solid line).

Figure of Merit

The common strategy of enhancing the figure of merit is increasing the power factor and minimizing the lattice thermal conductivity, where doping is playing a vital role in this regard. The effect of doping on the values of the figure of merit of the studied alloys is presented here. Figure 5.11 shows the figure of merit as a function of energy for GeSe and $Ge_{0.75}S_{0.25}Se_{0.75}Te_{0.25}$ at 300 K and 600 K. The figure of merit is found to decrease upon doping of the GeSe alloy by 33% and 26% at 300 K and 600 K, respectively. This result can be attributed to the behavior of the electronic thermal conductivity by introducing dopant to the material (see Figure 5.12). The figure shows a significant increase in the electronic thermal conductivity of $Ge_{0.75}S_{0.25}Se_{0.75}Te_{0.25}$ in comparison to GeSe. The figure shows that the electronic thermal conductivity is zero around the band gap in

GeSe, while this value increases to around 5 (W/mKs) in the case of $Ge_{0.75}S_{0.25}Se_{0.75}Te_{0.25}$ alloy.

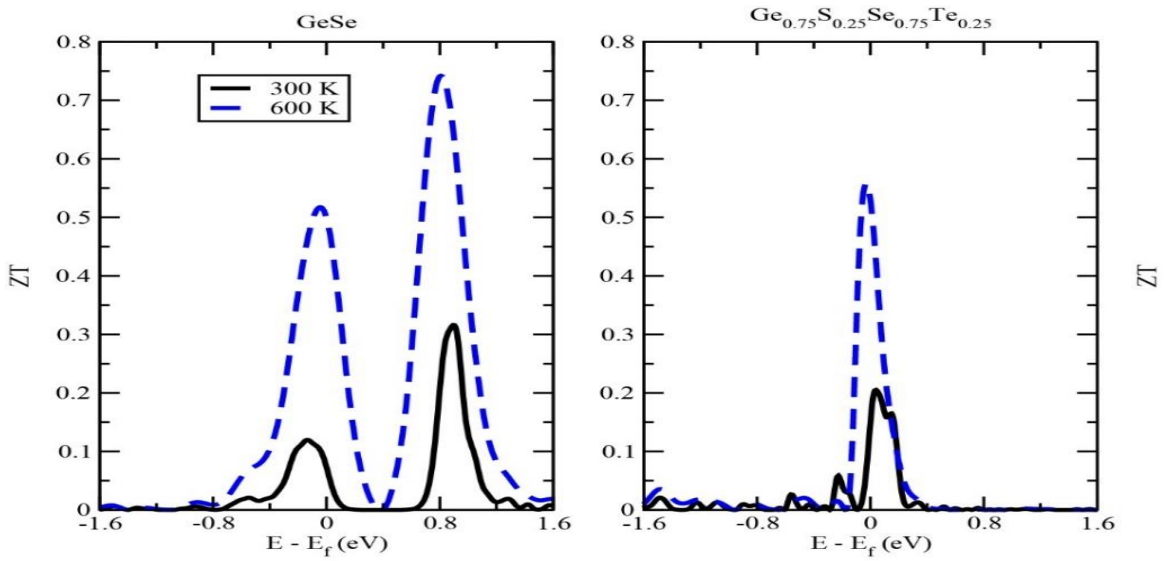

Figure 5.11. Figure of merit as a function of energy for GeSe (left panel) and $Ge_{0.75}S_{0.25}Se_{0.75}Te_{0.25}$ (right panel) at 300 K (solid line) and 600 K (dashed line).

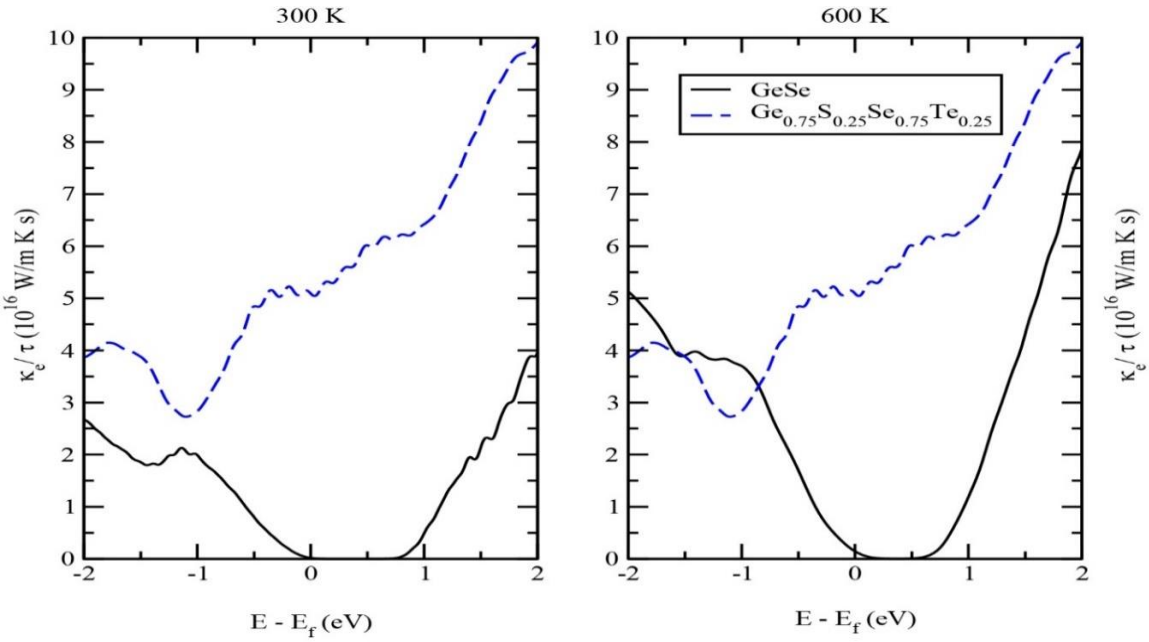

Figure 5.12. Electronic thermal conductivity as a function of energy for GeSe (solid line) and $Ge_{0.75}S_{0.25}Se_{0.75}Te_{0.25}$ (dashed line) at 300 K (left panel) and 600 K (right panel).

5.4 Summary

The electronic band structure and the thermoelectric properties of bulk orthorhombic GeS and GeSe were evaluated using density functional theory and Boltzman transport theory. The band gaps were found to be direct in the case of GeS and indirect for GeSe with values of 1.23 eV and 0.82 eV, respectively. The power factor of GeSe shows higher values by adding S on Ge site and adding Te on Se site than the case of GeS alloy. Introducing dopants to GeSe changes the orthorhombic structure to a simple monoclinic. As a result, the thermoelectric properties of these materials, including the Seebeck coefficient, electrical conductivity, and power factor at 300 K and 600 K for $Ge_{(1-x)}\,S_x\,Se_{(1-x)}Te_x$ (x=0.0, 0.25, 0.50, and 0.75) was studied. The highest power factor is predicted for the case of $Ge_{0.75}S_{0.25}Se_{0.75}Te_{0.25}$. The calculated lattice thermal conductivity of GeSe at 300 K is 1.78 W/mK, which decreases to 0.74 for the case of $Ge_{0.75}S_{0.25}Se_{0.75}Te_{0.25}$. However, these improvements in the power factor and lattice thermal conductivity did not result in a higher figure of merit for $Ge_{0.75}S_{0.25}Se_{0.75}Te_{0.25}$. This decrease can be attributed to that fact that doping increases the electrical conductivity, so inevitably it increases electronic thermal conductivity (κ_e), that leads to a lower value of the figure of merit.

Chapter 6: Conclusion

First principle calculations were performed to investigate the effect of polar order strength on the thermoelectric properties of GeTe alloy in its rhombohedral structure. Different magnitudes of polarization were found to affect the thermoelectric properties to a large extent. In particular, polar structures with higher polarization tend to show higher thermoelectric efficiencies. Thus, it is shown that polarization engineering is an important factor in designing efficient thermoelectric devices. In particular, it was proposed that high thermoelectric performance could be achieved by growing epitaxial GeTe films that are bi-axially compressed in the directions perpendicular to the polar axis in order to achieve larger polarization states.

The structural and electronic properties of GeS and GeSe were studied using DFT. Due to the better transport properties in GeSe, the effect of different concentration of dopant ($Ge_{(1-x)}S_xSe_{(1-x)}Te_x$ (x=0.0, 0.25, 0.5, 0.75)) were investigated in GeSe. Higher power factor and electrical conductivity were predicted for $Ge_{0.75}S_{0.25}Se_{0.75}Te_{0.25}$ at 300 K and 600 K. The addition of impurities to the material results in a 60% decrease of the lattice thermal conductivity and a significant increase of the power factor. However, these improvements did not lead to an enhancement in the value of the figure of merit of the doped $Ge_{0.75}S_{0.25}Se_{0.75}Te_{0.25}$ alloy as compared to the parent GeSe alloy.

References

[1] M. Morini, M. Pinelli, P. R. Spina, and M. Venturini, Applied Energy **112**, 205 (2013).

[2] C. Haddad, C. Périlhon, A. Danlos, M.-X. François, and G. Descombes, Energy Procedia **50**, 1056 (2014).

[3] A. Montecucco, J. R. Buckle, and A. R. Knox, Applied Thermal Engineering **35**, 177 (2012).

[4] J. Siviter, A. Montecucco, and A. R. Knox, Applied Energy **140**, 161 (2015).

[5] R. J. Goldstein,W.E. Ibele, S.V. Patankar, T.W. Simon, T.H. Kuehn, P.J. Strykowski, K.K. Tamma, J.V. R. Heberlein, J.H. Davidson, J. Bischof, F.A. Kulacki, U. Kortshagen, S. Garrick, V. Srinivasan, K. GhoshR Mittal, International Journal of Heat and Mass Transfer **53**, 4397 (2010).

[6] X. Liu, C. Li, Y. D. Deng, and C. Q. Su, International Journal of Electrical Power & Energy Systems **67**, 510 (2015).

[7] Z. Liu, C. Davis, W. Cai, L. He, X. Chen, and H. Dai, Proceedings of the National Academy of Sciences **105**, 1410 (2008).

[8] W. Liu, Q. Jie, H. S. Kim, and Z. Ren, Acta Materialia **87**, 357 (2015).

[9] B. Hamad, Journal of Materials Science **51**, no.24, 10887 (2016).

[10] B. Hamad, Journal of Electronic Materials **46**, 6595 (2017).

[11] S. Twaha, J. Zhu, Y. Yan, and B. Li, Renewable and Sustainable Energy Reviews **65**, 698 (2016).

[12] J. Lai and A. Majumdar, Journal of Applied Physics **79**, 7353 (1996).

[13] Y. Z. Pei, X. Y. Shi, A. LaLonde, H. Wang, L. D. Chen, and G. J. Snyder, Nature **473**, 66(2011).

[14] A. Zolriasatein, X. Yan, E. Bauer, P. Rogl, A. Shokuhfar, and S. Paschen, Materials & Design **87**, 883 (2015).

[15] G. J. Tan, L.-D. Zhao, F. Shi, J. Doak, S.-H. Lo, H. Sun, C. Wolverton, V. Dravid, C. Uher, and M.-G. Kanatzidis, Journal of the American Chemical Society **136**, 7006 (2014).

[16] A. Polozine, S. Sirotinskaya, and L. Schaeffer, Materials Research-Ibero-American Journal of Materials **17**, 1260 (2014).

[17] A. Bali, E. Royanian, E. Bauer, P. Rogl, and R. Chandra Mallik, Journal of Applied Physics **113**, 123707 (2013).

[18] Z. H. Dughaish, Physica B: Condensed Matter **322**, 205 (2002).

[19] J. Perez Taborda, O. Caballero-Calero, and M. Martín-González, *Silicon-Germanium (SiGe) Nanostructures for Thermoelectric Devices: Recent Advances and New Approaches to High Thermoelectric Efficiency*, (InTechOpen, London, 2017),z Chapter 8, p. 25.

[20] W. Shi, M. Gao, J. Wei, J. Gao, C. Fan, E. Ashalley, H. Li, and Z. Wang, Advanced Science **5**, 1700602 (2018).

[21] N. Moultif, A. Divay, E. Joubert, and O. Latry, in *Reliability of High-Power Mechatronic Systems 2*, edited by A. El Hami, D. Delaux, and H. Grzeskowiak (First published 2017 in Great Britain and the United States by ISTE Press Ltd and Elsevier Ltd, 2017), p. 241.

[22] G. S. Nolas, J. Sharp, and H. J. Goldsmid, *Thermoelectrics : Basic Principles and New Materials Developments* (Springer, Berlin; New York, 2010) pp. 1-14.

[23] J. R. Szczech, J. M. Higgins, and S. Jin, Journal of Materials Chemistry **21**, 4037 (2011).

[24] A. F. Ioffe and L. Infosearch, *Semiconductor Thermoelements and Thermoelectric Cooling* (Infosearch Ltd, London, 1957) pp. 5-7.

[25] N. M. Ravindra, B. Jariwala, A. Bañobre, and A. Maske, *Thermoelectrics Fundamentals, Materials Selection, Properties, and Performance* 2019), p. 2.

[26] D. Nemir and J. Beck, Journal of Electronic Materials **39**, 1897 (2010).

[27] M. Telkes, Journal of Applied Physics **18**, 1116 (1947).

[28] M. Abedlhafd, S. Izman, A. Noor, U. Basheer, and S. Rajoo, *A review of Thermoelectric p-type Ca 3 Co 4 O 9 Nanostructured Ceramics for Exhaust Energy Recovery*, Conference Paper, 2nd International Symposium on Engine Boosting and Energy Recovery September 11-13, 2017, Kuala-Lumpur, Malaysia, (September 2017), p. 4.

[29] J. C. Slater, Physical Review **81**, 385 (1951).

[30] H. Eschrig, *The Fundamentals of Density Functional Theory* (Teubner, Stuttgart; Leipzig, 1996), Chapter 4, pp. 74-98.

[31] E. K. U. Gross, R. M. Dreizler, *Density Functional Theory: An Approach to the Quantum Many Body Problem* (Berlin: Springer-Verlag, 1990), pp. 4-9.

[32] W. Kohn and L. J. Sham, Physical Review **140**, A1133 (1965).

[33] P. A. M. Dirac, Mathematical Proceedings of the Cambridge Philosophical Society **26**, 376 (1930).

[34] D. M. Ceperley and B. J. Alder, Physical Review Letters **45**, 566 (1980).

[35] J. P. Perdew, Physica B: Condensed Matter **172**, 1 (1991).

[36] J. P. Perdew and A. Zunger, Physical Review B **23**, 5048 (1981).

[37] A. V. Arbuznikov, Journal of Structural Chemistry **48**, S1 (2007).

[38] C. F. Fischer, J. B. Lagowski, and S. H. Vosko, Physical Review Letters **59**, 2263 (1987).

[39] T. Andersen, H. H. Andersen, P. Balling, P. Kristensen, and V. V. Petrunin, Journal of Physics B: Atomic, Molecular and Optical Physics **30**, 3317 (1997).

[40] O. V. Gritsenko, P. R. T. Schipper, and E. J. Baerends, The Journal of Chemical Physics **107**, 5007 (1997).

[41] A. D. Becke, The Journal of Chemical Physics **98**, 1372 (1993).

[42] A. D. Becke, Physical Review A **38**, 3098 (1988).

[43] L. H. Wu, X. Li, S. Y. Wang, T. S. Zhang, J. Yang, W. Q. Zhang, L. D. Chen, and J. H. Yang, Npg Asia Materials **9**, 7, e343 (2017).

[44] Z. Liu, Z. Liua, J. Sund, J. Mao, H. Zhub, W. Renb, J. Zhoua, Zh. Wange, D. J. Singhd, J. Suia, C.-W. Chub, and Z. Renb, Proceedings of the National Academy of Sciences **115**, 5332 (2018).

[45] J. Li, Z. Chen, X. Zhang, Y. Sun, J. Yang, and Y. Pei, NPG Asia Materials **9**, e353 (2017).

[46] H. L. Kagdada, P. K. Jha, P. Śpiewak, and K. J. Kurzydłowski, Physical Review B **97**, 134105 (2018).

[47] G. Z. Xing, J. F. Sun, Y. W. Li, X. F. Fan, W. T. Zheng, and D. J. Singh, Journal of Applied Physics **123**, 5, 195105 (2018).

[48] P.-C. Wei, C.-X. Cai, C.-R. Hsing, C.-M. Wei, S.-H. Yu, H.-J. Wu, C.-L. Chen, D.-H. Wei, D.-L. Nguyen, M. Chou, and Y.-Y. Chen, Scientific Reports **9**, 8616 (2019).

[49] T. Xing, Q. Song, P. Qiu1, Q. Zhang, X. Xia, J. Liao, R. Liu, H. Huang, J. Yang, S. Bai, D. Ren1, X. Shi, L. Chen, National Science Review **6**, 944 (2019).

[50] B. Srinivasan, A. Gelle, J. F. Halet, C. Boussard-Pledel, and B. Bureau, Materials **11**, 9, 2237 (2018).

[51] L. Xu, H.-Q. Wang, and J.-C. Zheng, Journal of Electronic Materials **40**, 641 (2011).

[52] B. Srinivasan, R. Gautier, F. Gucci, B. Fontaine, J.-F. Halet, F. Cheviré, C. Boussard-Pledel, M. J. Reece, and B. Bureau, The Journal of Physical Chemistry C **122**, 227 (2018).

[53] J. Dong, F.-H. Sun, H. Tang, J. Pei, H.-L. Zhuang, H.-H. Hu, B.-P. Zhang, Y. Pan, and J.-F. Li, Energy & Environmental Science **12**, 1396 (2019).

[54] Y. Jin, Y. Xiao, D. Wang, Z. Huang, Y. Qiu, and L.-D. Zhao, ACS Applied Energy Materials **2**, 7594 (2019).

[55] X. Y. Zhang, J. Li, X. Wang, Z. W. Chen, J. J. Mao, Y. Chen, and Y. Z. Pei, Journal of the American Chemical Society **140**, 15883 (2018).

[56] Đ. Dangić, A. R. Murphy, É. D. Murray, S. Fahy, and I. Savić, Physical Review B **97**, 224106 (2018).

[57] N. K. Abrikosov, V. F. Bankina, L. V. Poretskaya, L. E. Shelimova, and E. V. Skudnova, in *Semiconducting II–VI, IV–VI, and V–VI Compounds*, edited by N. K. Abrikosov, N. Khrisanfovich, V. F. Bankina, L. V. Poretskaya, L. E. Shelimova, E. V. Skudnova, (Springer US, Boston, MA, 1969), pp. 65-157.

[58] G. Kresse and J. Furthmüller, Physical Review B **54**, 11169 (1996).

[59] G. K. H. Madsen and D. J. Singh, Computer Physics Communications **175**, 67 (2006).

[60] W. Li, J. Carrete, N. A. Katcho, and N. Mingo, Computer Physics Communications **185**, 1747 (2014).

[61] X. Gao, K. Uehara, D. D. Klug, S. Patchkovskii, J. S. Tse, and T. M. Tritt, Physical Review B **72**, 125202 (2005).

[62] A. Togo and I. Tanaka, Scripta Materialia **108**, 1 (2015).

[63] K. Jeong, S. Park, D. Park, M. Ahn, J. Han, W. Yang, H.-S. Jeong, and M.-H. Cho, Scientific Reports **7**, 955 (2017).

[64] S.-J. Gong, F. Zheng, and A. M. Rappe, Physical Review Letters **121**, 017402 (2018).

[65] H. W. Shu, S. Jaulmes, R. Ollitrault-Fichet, and J. Flahaut, Journal of Solid State Chemistry **69**, 48 (1987).

[66] K. Shportko, S. Kremers, M. Woda, D. Lencer, J. Robertson, and M. Wuttig, Nature Materials **7**, 653 (2008).

[67] J.-H. Bahk and A. Shakouri, Applied Physics Letters **105**, 052106 (2014).

[68] Y. Wang, Y.-J. Hu, B. Bocklund, S.-L. Shang, B.-C. Zhou, Z.-K. Liu, and L.-Q. Chen, Physical Review B **98**, 224101 (2018).

[69] G. Ding, G. Gao, and K. Yao, Scientific Reports **5**, 9567 (2015).

[70] D. Parker and D. J. Singh, Physical Review B **85**, 125209 (2012).

[71] M. J. Graf, S. K. Yip, J. A. Sauls, and D. Rainer, Physical Review B **53**, 15147 (1996).

[72] Y. Gelbstein, O. Ben-Yehuda, E. Pinhas, T. Edrei, Y. Sadia, Z. Dashevsky, and M. P. Dariel, Journal of Electronic Materials **38**, 1478 (2009).

[73] A. Balandin and K. L. Wang, Physical Review B **58**, 1544 (1998).

[74] D. Campi, L. Paulatto, G. Fugallo, F. Mauri, and M. Bernasconi, Physical Review B **95**, 024311 (2017).

[75] H. Liu, X. Shi, F. Xu, L. Zhang, W. Zhang, L. Chen, Q. Li, C. Uher, T. Day, and G. Jeffrey Snyder, Nature Materials **11**, 422 (2012).

[76] S. Ishiwata, Y. Shiomi, J. S. Lee, M. S. Bahramy, T. Suzuki, M. Uchida, R. Arita, Y. Taguchi, and Y. Tokura, Nature Materials **12**, 512 (2013).

[77] L. D. Zhao, S. H. Lo, Y. S. Zhang, H. Sun, G. J. Tan, C. Uher, C. Wolverton, V. P. Dravid, and M. G. Kanatzidis, Nature **508**, 373 (2014).

[78] A. Samad, M. Noor-A-Alam, and Y.-H. Shin, Journal of Materials Chemistry A **4**, 14316 (2016).

[79] A. Shafique and Y.-H. Shin, Scientific Reports **7**, 506 (2017).

[80] J. O. Morales-Ferreiro, D. E. Diaz-Droguett, D. Celentano, and T. Luo, Frontiers in Mechanical Engineering **3**, 15 (2017).

[81] L. Shaabani, S. Aminorroaya-Yamini, J. Byrnes, A. Akbar Nezhad, and G. R. Blake, ACS Omega **2**, 9192 (2017).

[82] S. Hao, F. Shi, V. P. Dravid, M. G. Kanatzidis, and C. Wolverton, Chemistry of Materials **28**, 3218 (2016).

[83] J. Plata, D. Usanmaz, P. Nath, C. Toher, J. Carrete, M. Asta, M. de Jong, M. Buongiorno Nardelli, M. Fornari, S. Curtarolo, npj Computational Materials, **3**, 45, (2016).

[84] P. Mishra, H. Lohani, A. K. Kundu, R. Patel, G. K. Solanki, S. Krishnakumar, K. Menon, and B. Sekhar, Semiconductor Science and Technology **30** (2015).

[85] P. D. Antunez, J. J. Buckley, and R. L. Brutchey, Nanoscale **3**, 2399 (2011).

[86] P. Ramasamy, D. Kwak, D.-H. Lim, H.-S. Ra, and J.-S. Lee, Journal of Materials Chemistry C **4**, 479 (2016).

[87] L.-D. Zhao, L.-D, Zhao, G. Tan, S, Hao, J. He, Y, Pei, H. Chi, H. Wang, S. Gong, H. Xu, V.-P. Dravid, C. Uher, G.- J. Snyder, C. Wolverton, M.- G. Kanatzidis, Science **351**, 141 (2016).

[88] J.-i. Tani and H. Kido, Physica B-condensed Matter - PHYSICA B **364**, 218 (2005).

[89] F. Mouhat and F.-X. Coudert, Physical Review B **90**, 224104 (2014).

[90] R. F. Pierret, *Semiconductor Device Fundamentals* (Addison-Wesley Longman, Massachusetts, 2006), pp. 26-32.

[91] H. Xie, X. Gu, and H. Bao, *A Relaxation Time model for Efficient and Accurate Prediction of Lattice Thermal Conductivity*, arXiv:1811.09968v1, (2018).

[92] A. J. Hong, L. Li, R. He, J. J. Gong, Z. B. Yan, K. F. Wang, J. M. Liu, and Z. F. Ren, Scientific Reports **6**, 22778 (2016).

[93] H. Ma, C.-L. Yang, M.-S. Wang, X.-G. Ma, and Y.-G. Yi, Journal of Physics D: Applied Physics **52**, 255501 (2019).

[94] C. Dhakal, S. Aryal, R. Sakidja, and W.-Y. Ching, Journal of the European Ceramic Society **35**, 3203 (2015).

[95] M. Sist, C. Gatti, P. Nørby, S. Cenedese, H. Kasai, K. Kato, and B. B. Iversen, Chemistry – A European Journal **23**, 6888 (2017).

[96] X. Zhang, J. Shen, S. Lin, J. Li, Z. Chen, W. Li, and Y. Pei, Journal of Materiomics **2**, 331 (2016).

Appendices

Appendix A: Description of Research for Popular Publication

In recent years, population is growing, all the new technologies lead to untapped use of energy and, due to limited source of fossil fuels, these problems make the world less energy efficient. Global warming is another problem which made all scientists deeply worried. Since scientists started to make extensive research in the field of renewable energy, one of their solutions was thermoelectric materials.

What are thermoelectric materials? Thermoelectric materials are materials which convert wasted heat into electricity, by which either a temperature difference creates an electric potential, or an electric potential creates temperature difference. So thermoelectric materials play a critical role in reducing the dependence on fossil fuels and reduce greenhouse gas emissions and they can be considered as a green source of energy. Thermoelectric modules can be used in a wide range of applications. These applications range between consumer products such as beverage coolers and military products such as temperature regulators and missiles.

Is it an easy way to produce electricity from wasted heat? Imagine producing electricity from a car from by wasted heat that is produced by the exhaust pipe. Here a question should cross our mind! Are all materials appropriate for this goal? Different materials have different thermal properties. In our group, we try to find thermoelectric properties of different materials and introduce them to the world. In this way, these materials can be used in the right place. Maybe a material which is not good for beverage cooler can be the right choice for space vehicles or vice versa. Another thing that is investigated in our group is the thermoelectric properties of compounds. In this way, a material which is not a good candidate for our goals can be converted to a good candidate just by considering doping them with other elements.

But this not the whole story since we try to investigate different facets of materials, for example, the price, toxicity, and the effect of materials in our world. All in all, we do not want to solve a problem for the world and yet produce different problems. As a result, in this research field, the best candidate for designing thermoelectric generators or refrigerators are introduced, and their operating temperature is defined. In other words, a list of materials with their application and appropriate technique for different thermoelectric goals will be introduced by researchers who are working in our field to engineer for mass production.

Appendix B: Executive Summary of Newly Created Intellectual Property

The following list of new intellectual property items were created in the course of this research and should be considered from both a patent and commercialization perspective.

1. Considering polarization as a degree of freedom for studying thermoelectric properties of GeTe.
2. Doping GeSe with S on Ge-site and with Te on Se-site and showing the effect of doping on thermoelectric properties of GeSe.

Appendix C: Potential Patent and Commercialization Aspects of Listed Intellectual Property Items

C.1 Patentability of Intellectual Property (Could Each Item be Patented)

1. Effect of polar distortion on thermoelectric properties of GeTe were investigated computationally, these studies could not be patented
2. Doping GeSe with S on Ge-site and with Te on Se-site were investigated computationally, these studies could not be patented.

C.2 Commercialization Prospects (Should Each Item Be Patented)

NA

C.3 Possible Prior Disclosure of IP

NA

Appendix D: Broader Impact of Research

D.1 Applicability of Research Methods to Other Problems

This research deciphered the effect of polar distortion on the thermoelectric properties of GeTe and investigated the presence dopant on GeS and GeSe. These results can be used for choosing the appropriate material for thermoelectric generators or refrigerators. Materials that show slightly antisymmetric structure and lack of inversion symmetry can be a better candidate for thermoelectric goals. To increase the efficiency of GeS and GeSe for thermoelectric applications such as generators or refrigerators the incorporation of group III-IV elements as dopants is not a good technique for improving figure of merit in GeS and GeSe. Providing this information can save a lot of money and time from engineers and companies.

The computational methods that are used in this research, such as DFT, can be used in the study of complex systems to predict their behavior, synthesis-related systems, and processing parameters. The elastic constants matrix is a cheap technique to study the stability of different structures.

D.2 Impact of Research Results on U.S. and Global Society

The research proposed in this thesis is expected to help with the advancement of clean and renewable energy sources. By taking advantage of the Seebeck effect, it is possible to convert vibrational (heat) energy into electrical energy. This type of green energy could make it possible to reduce reliance of our society on fossil fuels. This can have positive effects on both the planet and economics while also increasing the stability of our society through the years by ensuring that our societies energies needs are maintained even after fossil fuels run out. This research can be used to assist manufacturers when choosing the appropriate material for thermoelectric generators or refrigerators. These generators are useful for power generation and can be used in spacecraft.

It can also be designed in such a way as to be used for cooling in electrical components.

D.3 Impact of Research Results on the Environment

Since the main source of energy in the world is fossil fuels and the main disadvantages of these resources is pollution, researchers around the world are looking for new sources of energy to decrease this dependency. In this study, by introducing materials with better thermoelectric properties and utilization of special methods such as polar distortion and elemental doping, the pathway to creating clean energy is facilitated.

Appendix E: Microsoft Project for MS MicroEP Degree Plan

Appendix F: Identification of All Software Used in Research and thesis Generation

Computer #1:

Model Number: Dell Precision Tower 3620

Serial Number: 8Z85XQ2

Location: PHYS244

Owner: Prof. Bothina (Hamad) Manasreh

Software #1:

Name: Ubuntu

Free license: Downloaded by Aida Sheibani.

Computer #2: Personal Laptop.

Model Number: P69G

Serial Number: 1MRR6L2

Owner: Aida Sheibani

Software #1:

Name: Cygwin 3.1.1

Free license: Downloaded by Aida Sheibani.

Software #2:

Name: Microsoft Office 365 Pro Plus-en-us

Purchased by: University of Arkansas

Software #3:

Name: XMGRACE

Free license: Downloaded by Aida Sheibani.

Software #4:

Name: VESTA

Free license: Downloaded by Aida Sheibani.

Software #5:

Name: Python 3.7.1

Free license: Downloaded by Aida Sheibani.

Computer #3: Physics Library.

Model Number: P69G

Serial Number: 1MRR6L2

Location: PHYS122

Owner: University of Arkansas

Software #1:

Name: Adobe illustrator

Free license: Downloaded by Aida Sheibani.

Appendix G: All Publications Published, Submitted and Planned

Submitted

1. Aida Sheibani, Charles Paillard, Abhiyan Pandit, Raad Haleoot, Laurent Bellaiche, and Bothina Hamad “Effect of the polar distortion on the thermoelectric properties of GeTe”, J. Phys. Condens. Matter.

Planned

1. Aida Sheibani, Raad Haleoot, and Bothina Hamad “Effect of the doping on the thermoelectric properties of GeSe”, J. Phys. Condens. Matter.

Presentations

1. Aida Sheibani, Charles Paillard, Raad Haleoot, and Bothina Hamad 2019 Investigation of the structural, electronic and thermoelectric properties of GeX (X= S, Se, Te) monochalcogenides Bulletin of the American Physical Society, APS March Meeting, Boston, MA, March 4 -8, 2019.